CrossMark

JM PAPERS

Simulation-based study of low-Reynolds-number flow around a ventilated cavity

Han Liu[1], **Zuoli Xiao**[2] **and Lian Shen**[1],†

[1]Department of Mechanical Engineering and St. Anthony Falls Laboratory, University of Minnesota, Minneapolis, MN 55455, USA

[2]State Key Laboratory for Turbulence and Complex Systems, College of Engineering, Peking University, Beijing 100871, PR China

Ventilated cavitating flows are investigated via direct numerical simulations, using a coupled level set and volume of fluid method to capture the interface between the air and water phases. A ventilated disk cavitator is used to create the cavity and is modelled by a sharp-interface immersed boundary method. The simulation data provide a comprehensive description of the two-phase flow and the air leakage and vortex shedding processes in the cavitating flow. The mean velocity of the air phase suggests the existence of three characteristic flow structures, namely the shear layer (SL), recirculating area (RA) and jet layer (JL). The turbulent kinetic energy (TKE) is concentrated in the JL in the closure region, and streamwise turbulent fluctuations dominate transverse fluctuations in both SL and JL. Budget analyses of the TKE show that the production term causes the TKE to increase in the SL due to the high velocity gradients, and decrease in the JL due to streamwise stretching effects. Air leakage and vortex shedding occur periodically in the closure region, and the one-to-one correspondence between these two processes is confirmed by the velocity and volume fluid spectra results, and the autocorrelation function of the air volume fraction. Moreover, the coherent flow structures are analysed using the spectral proper orthogonal decomposition method. We identify several fine coherent structures, including SL_{KH} induced by the Kelvin–Helmholtz instability, SL_{out} associated with large-scale vortex shedding, SL_{in} associated with small-scale vortex shedding, and SL_r associated with upstream turbulent convection. The present study complements previous research by providing detailed descriptions of the turbulent motions associated with the violent mixing of air and water, and the complex interactions between different characteristic structures in cavitating flows.

Key words: cavitation, multiphase flow, bubble dynamics

† Email address for correspondence: shen@umn.edu

1. Introduction

Natural cavitation occurs when the local static pressure in a flow becomes lower than the vapour pressure, leading to the formation of bubbles or cavities. Cavitation effects can reduce skin friction drag considerably, allowing underwater vehicles to achieve high speeds, especially when the gas bubbles are sufficiently large and encompass most of the surface (or the entire surface) of a vehicle travelling through water. In practice, large cavities are rarely generated by natural cavitation effects because of the technical challenges faced when a vehicle accelerates from an initially non-cavitating state to a cavitating state, such as the unsteady effects caused by buffeting and surface deformation vibrations. On the other hand, artificial ventilation, which involves blowing a non-condensable gas to create a cavity, can overcome many of these difficulties. However, a deep understanding of the internal structures of ventilated cavities and their interactions with turbulent flows is necessary to design appropriate high-speed underwater vehicles (Semenenko 2001).

In the ventilated cavitation process, air escapes from the cavity through the rear sealing zone, which is also known as the closure part. Violent flow mixing between water and air occurs in this region. Two main closure modes have been identified in previous studies, namely the re-entrant jet (RJ) and the twin vortex (TV). The RJ closure mode occurs when the gravitational effect is less significant than the advection effect. In this case, the rear portion of the cavity is filled with periodically expelled foams that are in the form of doughnut-like axisymmetric vortices (see e.g. Campbell & Hilborne 1958). The TV closure mode features a pair of vortex tubes at the rear of the cavity and usually occurs when the gravitational effect is dominant (Cox & Clayden 1956). The TVs in the ventilated cavity have similar geometries to the TVs in prolate spheroids at certain angles of attack. However, in flows other than the inclined prolate spheroid case, TVs are generated by vortex stretching and tilting processes, while in the cavitating flow, TVs are generated by gravitational effects, which leads to the lift up of the cavity in the streamwise direction, resulting in a velocity difference between the upper and lower cavity surfaces and the subsequent flow separation (see e.g. Wang *et al.* 2021*b*).

Most previous studies focused on establishing connections among the dimensionless parameters governing these closure behaviours (e.g. Epshtein 1973; Logvinovich 1973; Spurk 2002; Kinzel, Lindau & Kunz 2009; Wu *et al.* 2019) and understanding the mechanisms that lead to the variations in the closure modes under different flow conditions (e.g. Semenenko 2001; Zhou *et al.* 2010; Kawakami & Arndt 2011; Ahn *et al.* 2017; Wu *et al.* 2019). While considerable knowledge on closure behaviours has been gained in previous studies, few studies have investigated the turbulence dynamics near the closure part in ventilated cavities, which is the focus of this paper.

Turbulence near the closure is important for understanding the mechanisms governing air and water mixing, air leakage and vortex shedding in ventilated cavitating flows. It is also the physical foundation for the development of turbulence models in cavitation flow applications. However, although some studies have discussed turbulence, most previous works focused on qualitative descriptions of turbulent flows and unsteady behaviours and did not analyse cavity–turbulence interactions quantitatively. In particular, few studies have explored the details of the vortex dynamics, the distribution of turbulent kinetic energy, the energy transfer budgets, or the distribution of Reynolds stresses near the closure part of the ventilated cavity. These topics are difficult to investigate experimentally due to the challenges in obtaining non-intrusive measurements on the turbulence dynamics in the air–water mixing region. For computational works, it is challenging to simulate accurately multiphase flows with large density ratios and turbulent motions with wide

scale ranges. Early theoretical works on cavity–turbulence interactions were based on statistical theories (e.g. Plesset & Prosperetti 1977; Rood 1991). Later studies focused on more detailed descriptions of cavity–turbulence interactions. For example, Callenaere *et al.* (2001) investigated RJ instability, demonstrating that the pressure gradient in the cavity sealing zone has a strong influence on the closure and local turbulence intensity. As reviewed in Arndt (2002), cavitation can influence vortex dynamics and generate turbulence in complex ways, and cavities are sources of vorticity near the closure region. Recently, Gnanaskandan & Mahesh (2016) conducted large-eddy simulations (LES) of cavitating flows over circular cylinders. They found that cavitation can attenuate turbulence near the wake of the cavity. This result was confirmed by Karathanassis *et al.* (2018). Koukouvinis *et al.* (2017) analysed cavitating flows inside orifices using experimental techniques and numerical methods, and found that the turbulence in the orifice region is affected by cavitation structures. More specifically, turbulence is dampened in dense cavitation regions and enhanced in cavitation collapse regions. Moreover, they found that turbulence is suppressed in the presence of well-established cavitation. Barbaca *et al.* (2019) investigated the influence of the free-stream Reynolds number and Froude number on cavity closure dynamics, and made a comparison between ventilated and naturally cavitating flows. They applied shadowgraphy and proper orthogonal decomposition (POD) analysis techniques to study wake flows, noting that the free-stream velocity influences the size and number of shed structures in the turbulent mixing region of the ventilated cavitating flow. Wang *et al.* (2021*a*) studied ventilated cavitating flows in the wake of circular cylinders, through numerical simulations. Their primary finding on turbulence dynamics is that as the gas entrainment increases, the turbulence intensity near the closure part decreases, together with a decrease in the number of bubbles.

Moreover, several previous studies have revealed that coherent flow structures play important roles in the turbulence dynamics of ventilated cavitation (e.g. Dittakavi, Chunekar & Frankel 2010; Wang *et al.* 2018; Wu *et al.* 2021). However, we still lack an understanding about how the coherent structures near the closure part of the ventilated cavity are linked to the turbulence dynamics, and what roles these coherent structures play during the air leakage and vortex shedding processes. To address this knowledge gap, in the present work, we employ a spectral proper orthogonal decomposition (SPOD) method to identify the coherent structures near the closure region in ventilated cavitating flows to efficiently describe the dynamics with a modal decomposition approach. The SPOD method is a variant of the POD approach proposed originally by Lumley (1967, 1970), which extracts a set of eigenmodes to develop a least-squares representation of a given set of flow data. One of the POD forms described by Sirovich (1987) has been used widely in the literature (e.g. Aubry 1991; Berkooz, Holmes & Lumley 1993; Meyer, Pedersen & Özcan 2007; Hellström, Ganapathisubramani & Smits 2015). This POD approach aims to identify spatially orthogonal modes by decomposing the spatial correlation tensor under the assumption that each instantaneous snapshot is a temporally independent realization, and is referred to as the spatial-only POD approach by Towne, Schmidt & Colonius (2018). In contrast, the SPOD method extracts modes, each of which oscillates at a specific frequency, by decomposing the cross-spectral density tensor. As a result, the SPOD method accounts for the temporal coherence in the snapshots (Towne *et al.* 2018). The SPOD approach has been applied to identify coherent structures in various flow settings. For example, Nidhan, Schmidt & Sarkar (2022) used SPOD to extract and analyse coherent structures in the turbulent wake of a disk, and revealed their relationships with buoyancy, vortex shedding, and unsteady internal gravity waves. Abreu *et al.* (2020) employed SPOD

to analyse coherent structures in a turbulent pipe flow. Li *et al.* (2021) used the SPOD method to investigate coherent structures near ground vehicles and their aerodynamic features. Ghate, Towne & Lele (2020) reconstructed the turbulence field by combining the SPOD method with a physics-based enrichment algorithm that uses spatiotemporally localized Gabor modes to represent turbulence in the inertial subrange. Kadu *et al.* (2020) employed SPOD to elucidate dynamically important modes in unconfined coaxial jets. Schmidt *et al.* (2018) examined turbulence structures in jets using the SPOD approach, and connected the wavepackets observed at different locations to the flow dynamics. Nekkanti & Schmidt (2021) demonstrated several applications of the SPOD method in a turbulent jet flow setting, including flow field reconstruction, denoising, frequency–time analysis, and prewhitening. In the present paper, we employ SPOD to analyse coherent flow structures in ventilated cavitating flows for the first time.

Our study utilizes a direct numerical simulations (DNS) approach that indicates sufficient resolution to resolve the key dynamics associated with closure and entrainment mechanisms. As computational power has increased, computational fluid dynamics (CFD) has become a powerful tool in cavitation studies to obtain detailed descriptions of three-dimensional flow fields. In addition to the works by Gnanaskandan & Mahesh (2016) and Wang *et al.* (2021*a*) reviewed above, Uhlman & James (1989) and Abraham, James & Ivan (2003) simulated steady cavitating flows numerically using a boundary element method. Wang & Ostoja-Starzewski (2007) investigated the cavitating flow induced by natural cavitation using both Reynolds-averaged Navier–Stokes (RANS) simulations and LES, treating the two fluid phases as a coherent fluid system in the simulations. Senocak & Shyy (2002) simulated unsteady cavitating flows using a two-phase RANS method. Kunz *et al.* (2000) proposed a preconditioned Navier–Stokes method to simulate cavitation dynamics. Lindau *et al.* (2015) conducted RANS simulations and LES based on a finite-volume method to study pulsation phenomena in cavities. Kinzel (2008) developed a numerical method for compressible cavitating flows by combining the level set interface capturing method and the overset mesh method, thereby improving the accuracy and stability of the simulation. This numerical tool has also been employed to investigate the air entrainment process and closure modes of cavitating flows.

The present paper presents a DNS study of ventilated cavitating flows, focusing on the interaction between cavity and turbulence, including comprehensive analyses of two-phase turbulent flows, internal structures and statistical quantities. We investigate the turbulence dynamics in various cavity structures by analysing the processes of air leakage, vortex shedding, and oscillations in the ventilated cavitating flow. The aim of this study is to address the following questions. (1) What are the characteristic flow structures inside a cavity? (2) What is the physical mechanism responsible for generating turbulence near the closure region? (3) What roles do the characteristic structures near the closure region play in the transport of turbulent kinetic energy (TKE)? (4) What flow process governs the air leakage and vortex shedding in the closure region?

The remainder of this paper is organized as follows. First, § 2 introduces the governing equations, numerical method and simulation approach. Then the time-averaged statistics of the flow field, including the mean flow, Reynolds stresses and vortex dynamics, are presented in § 3. Next, the TKE and its budget in the cavity are discussed in § 4. Moreover, § 5 investigates air leakage and its correlation with coherent vortex structures. The coherent structures near the closure region are analysed using the SPOD method in § 6. Furthermore, § 7 discusses the assessment of lower-Reynolds-number DNS simulations for insights into ventilated cavitating flows. Finally, the conclusions are summarized in § 8.

2. Problem set-up and numerical methods

In this section, we first introduce the problem set-up and governing equations in § 2.1. Then, in § 2.2, we describe the numerical methods employed to simulate the air and water flows and track the dynamic air–water interface. Finally, we present the computational parameters in § 2.3.

2.1. *Problem set-up and governing equations*

In our mechanistic study of ventilated cavitation and the turbulent flow therein, we consider a computational setting with a ventilating cavitator located inside a rectangular water tunnel with uniform water inflow from the inlet. In the present simulation, we consider only the case in which the mainstream velocity is not very high so that the natural cavitation regime is not attained. In other words, the influence of natural cavitation effects on the cavity is not considered in our computational setting. Figure 1(*a*) shows the computational domain in our coordinate system, with *x*, *y* and *z* denoting the streamwise, vertical and transverse directions, respectively. The water flows through the inlet with velocity U_∞ in the *x* direction, passes the cavity, and exits through the outlet. In the simulation, a Dirichlet boundary condition is imposed at the inlet, and a convective boundary condition is applied at the outlet (Lodato, Domingo & Vervisch 2008).

Figure 1(*b*) shows a schematic of the cavity, with the cavitator and ventilation source indicated. The cavitator, which is located on the central axis at $x_c = 30d_c$, is a circular disk with diameter d_c and thickness $0.3d_c$. We use a spherical source region with diameter $0.6d_c$ that is located $1d_c$ behind the disk to generate ventilation in the simulation. This numerical treatment overcomes the numerical difficulty of representing a practical small air ventilation configuration with limited grid resolution. More numerical details are provided in § 2.2. In our experiments and applications, air is ventilated out through a vent port mounted on the strut, which is used to support the cavitator. The shape and position of the vent port and the air ventilation direction can influence the cavity (Semenenko 2001). Because the aim of the present work is to elucidate the fundamental mechanisms of the cavity, the complex object and vent settings can be replaced by a simplified model without loss of generality in this mechanistic study.

In the simulation, a fluid system with variational densities and viscosities is used to treat the air and water simultaneously. The fluid motion is governed by the incompressible Navier–Stokes equations and continuity equation as follows:

$$\frac{\partial u_i}{\partial t} + \frac{\partial (u_i u_j)}{\partial x_j} = -\frac{1}{\rho}\frac{\partial p}{\partial x_i} + g_i + \frac{1}{\rho}\frac{\partial \sigma_{ij}}{\partial x_j} + \frac{1}{\rho}T_i, \tag{2.1}$$

$$\frac{\partial u_j}{\partial x_j} = 0. \tag{2.2}$$

In the above equations, x_i ($i = 1, 2, 3$) denote the Cartesian coordinates (x, y, z), u_i are the (u, v, w) components of the flow velocity, ρ is the density of the fluid, p is the dynamic pressure, g_i ($i = 1, 2, 3$) indicate the components of the gravitational acceleration, $\sigma_{ij} = \mu(\partial u_i/\partial x_j + \partial u_j/\partial x_i)$ ($i, j = 1, 2, 3$) denote the components of the stress tensor, T_i ($i = 1, 2, 3$) denote the components of the surface tension at the air–water interface, and μ is the dynamic viscosity.
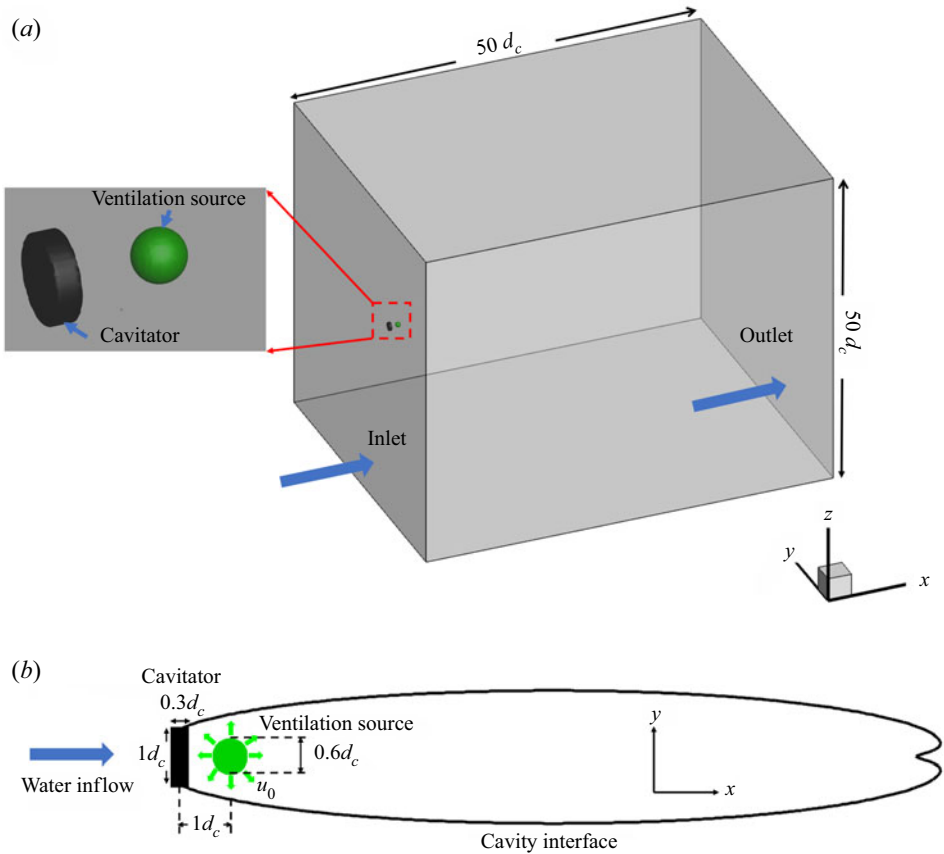
Figure 1. Schematic of the simulation set-up: (*a*) computational domain, and (*b*) cavity, cavitator and ventilation source. The blue arrow on the left of the cavitator indicates the water inflow direction. The green arrows indicate the air ventilation directions.

2.2. *Numerical methods*

The momentum equations (2.1) are spatially discretized using the second-order central difference scheme. Several considerations were noted when we adopted this scheme. First, this scheme is simple to implement and requires less computational time per step than other approaches. Furthermore, this scheme works robustly with our approach for solving the Poisson equation. Moreover, the short stencil of this scheme allows us to implement the immersed boundary method and the coupled level set and volume-of-fluid (CLSVOF) method, and increases the numerical robustness. Finally, this scheme is numerically non-dissipative, which enables the DNS to resolve turbulent motions over a wide range of scales. The second-order Runge–Kutta (RK2) method is employed for time advancement. To enforce the continuity equation (2.2), the fractional-step method (Kim & Moin 1985) is utilized at each substep of the RK2 method. The pressure is obtained by solving the Poisson equation as follows:

$$\frac{\partial}{\partial x_i}\left(\frac{1}{\rho}\frac{\partial p}{\partial x_i}\right) = \frac{1}{\Delta t}\left(\frac{\partial u_j^*}{\partial x_j} - S\Phi\right), \tag{2.3}$$

where Δt is the time step, and u^* is the intermediate velocity in the projection method without adding the pressure gradient in (2.1). Moreover,

$$S = \frac{u_0 4\pi (0.5 d_s)^2}{\frac{4}{3}\pi (0.5 d_s)^3} = \frac{10 u_0}{d_c} \tag{2.4}$$

is the divergence constant in the ventilation source, Φ is a Heaviside function that equals 1 inside the ventilation source and 0 otherwise, $d_s = 0.6 d_c$ is the diameter of the ventilation source, and u_0 is the uniform air ventilation speed (sketched in figure 1a). The uniform air ventilation speed u_0 can be calculated using the air entrainment coefficient $C_q = Q/(U_\infty d_c^2)$, where Q is the air ventilation rate:

$$u_0 = \frac{C_q (U_\infty d_c^2)}{4\pi (0.5 d_s)^2} = \frac{25 C_q U_\infty}{9\pi}. \tag{2.5}$$

Equation (2.3) is a Poisson equation with a large matrix because it involves grid points in three dimensions. The direct inversion of such a large matrix is computationally prohibitive. As a result, this matrix needs to be solved with an iterative method. Moreover, the simulations must be performed on large parallel computers, which increases the computational costs. The portable extensible toolkit for scientific computation (PETSc) package has been applied in many previous studies (see e.g. Balay *et al.* 2017; Yang, Deng & Shen 2018; Gao, Deane & Shen 2021b) and has been shown to be computationally efficient and robust in solving the Poisson equation. Thus this package is adopted in this study.

The air–water interface is captured using the CLSVOF method (Sussman & Puckett 2000). The level set function ψ describes the distance to the air–water interface, with positive and negative values in the water and air, respectively. The zero value of ψ corresponds to the interface. The norm of the gradient of ψ is identically unity, i.e.

$$|\nabla \psi| = 1. \tag{2.6}$$

The governing equation of ψ takes the form

$$\frac{\partial \psi}{\partial t} + u_j \frac{\partial \psi}{\partial x_j} = 0, \tag{2.7}$$

which can be spatially discretized by applying a second-order essential non-oscillatory scheme (Shu & Osher 1989), and integrated over time with a second-order operator-splitting method. A reinitialization procedure (Min 2010) is employed to ensure that the advected ψ is the signed-distance function described by (2.6).

The air and water phases are recognized by their density and viscosity, which are determined based on the level set function ψ as

$$\rho = H(\psi)\,\rho_w + (1 - H(\psi))\,\rho_a, \tag{2.8}$$

$$\mu = H(\psi)\,\mu_w + (1 - H(\psi))\,\mu_a, \tag{2.9}$$

where $H(\psi)$ is the Heaviside function, ρ_w and ρ_a are the densities of water and air, and μ_w and μ_a are the dynamic viscosities of water and air, respectively. In the simulation, these

values are smoothed near the air–water interface as

$$H(\psi) = \begin{cases} 0, & \psi < -\epsilon, \\ \dfrac{1}{2}\left[1 + \dfrac{\psi}{\epsilon} + \dfrac{1}{\pi}\sin\left(\dfrac{\psi\pi}{\epsilon}\right) \right], & |\psi| \le \epsilon, \\ 1, & \psi > \epsilon. \end{cases} \tag{2.10}$$

Here, ϵ is the half-thickness of the diffusion region. According to our previous research (Yang *et al.* 2018), ϵ is set to three times the smallest grid size.

The volume-of-fluid (VOF) method, which captures the interface according to the colour function ϕ, is implemented to enforce mass conservation for each fluid phase. Here, ϕ is the volume fraction of water in a grid cell, which is equal to 1 in the water, and 0 in the air. The governing equation of ϕ is

$$\frac{\partial \phi}{\partial t} + \frac{\partial(u_j\phi)}{\partial x_j} = 0, \tag{2.11}$$

which is solved by using the conservative VOF method (Weymouth & Yue 2010).

The CLSVOF method proposed by Sussman, Smereka & Osher (1994) is used to couple ψ and ϕ. Before solving the advection equations (2.7) and (2.11) in each time integration substep, the level set function ψ is used to determine the normal direction of the interface in each grid cell. The coefficients in the normal direction are calculated by minimizing a weighted summation of the distances from the surrounding nodes to the interface. After obtaining the interface function in each grid cell, a piecewise linear interface calculation algorithm is used to calculate the flux of ϕ, which is used to advect ϕ. Then ϕ is used to adjust the values of the advected ψ near the interface to maintain mass conservation. Details on the CLSVOF algorithm and its applications in a variety of multifluid problems can be found in previous papers by our group, including Hu *et al.* (2012), Yang *et al.* (2017, 2018) and Gao *et al.* (2021*a*).

To capture the effect of the submerged cavitator on the flow, the immersed boundary method (Mittal & Iaccarino 2005; Kim & Choi 2019) is employed in the flow solver (Cui *et al.* 2018), wherein an appropriate body force is applied on the grid points near the cavitator surface to enforce the no-slip boundary condition. The immersed boundary method can be applied to resolve solid bodies in Cartesian grids instead of in body-fitted grids, thereby simplifying the algorithm and reducing the computational time. Figure 2 shows a typical instantaneous cavity in our simulation. Several ventilated cavitation components are indicated in the figure, including the interface, which is the air–water boundary, the front part, which is the main body of the cavity, and the closure part, which is the rear portion of the cavity from which air escapes and where the two phases mix violently. To further illustrate these dynamics, a supplementary movie is provided. It offers a real-time visual representation, specifically highlighting the violent mixing process and the escape of air packets from the closure part of the cavity (see supplementary movie available at https://doi.org/10.1017/jfm.2023.431).

2.3. *Computational parameters*

The $50d_c \times 50d_c \times 50d_c$ (length $\times$ height $\times$ width) computational domain is discretized using a stretched Cartesian mesh grid. The length of the computational domain is enlarged to the maximal possible range according to the available computational resources to ensure that the outlet boundary condition has an insignificant effect on the ventilated cavitation. We conducted three simulations using different mesh grids with various resolutions,
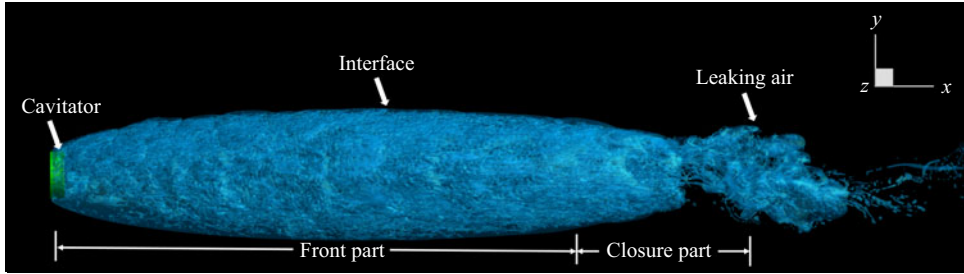
Figure 2. Visualization of a cavity with various components. The isosurfaces of $\psi = 0$ (blue) and the disk cavitator (green) are plotted.
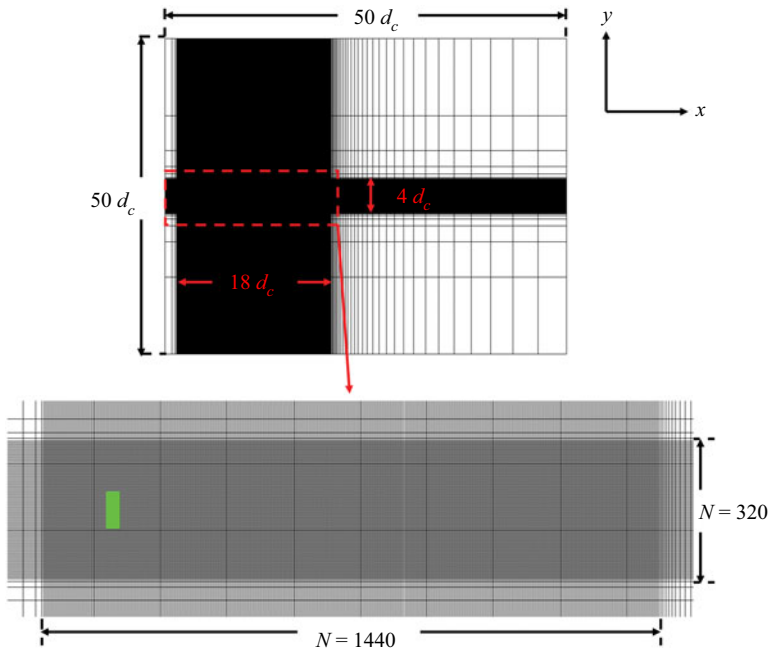

Figure 3. Sketch of the mesh grid M_3 on the midplane of the computational domain, where the red dashed rectangle indicates the refined mesh region, and the green rectangle denotes the disk cavitator. For illustration purposes, only one of every four grid points in each direction is plotted.

which are denoted as M_1, M_2 and M_3. The grids M_1, M_2 and M_3 have $400 \times 96 \times 96$, $800 \times 192 \times 192$ and $1600 \times 384 \times 384$ grid points, respectively. The mesh grid is refined around the cavitator and is coarsened progressively along the $(x - x_c)/d_c < 4$ and $(x - x_c)/d_c > 18$ directions (figure 3). Table 1 lists the grid resolution in terms of the minimum cell size Δ_{min}, the time step Δt_f, the grid number, the number of cores used for the parallel computing, and the total core-hours spent on the simulations.

The M_1 simulation was performed until the size of the cavity became statistically stable at approximately $t_c = 700 d_c/U_\infty$. The simulation was continued for $t_c = 500 d_c/U_\infty$ to obtain the flow statistics. Then the M_2 and M_3 simulations were initialized by interpolating the M_1 simulation flow field data at $t = t_c$ to the mesh grids with higher resolutions.

The flow statistics of the M_2 and M_3 simulations are calculated after transient periods $t = 3.8 d_c/U_\infty$ and $t = 5.2 d_c/U_\infty$, respectively, during which the flows adjust to the

Mesh grids and runs	d_c/Δ_{min}	$\Delta t_f\, U_\infty/d_c$	No. of cells	No. of cores	Total core-hours
M_1	20	2.0×10^{-3}	3.69×10^6	128	$\sim 8 \times 10^4$
M_2	40	2.0×10^{-3}	2.95×10^7	1024	$\sim 1 \times 10^5$ (started from $t = t_c$)
M_3	80	1.0×10^{-3}	2.36×10^8	8192	$\sim 3 \times 10^6$ (started from $t = t_c$)

Table 1. Summary of simulation runs.

statistical stationary status under the new grid resolutions. The flow statistics of the M_2 and M_3 simulations are calculated over durations $t = 480d_c/U_\infty$ and $t = 440d_c/U_\infty$, respectively.

The time step is set based on the stability criteria (Ling *et al.* 2019)

$$\Delta t \le \Delta t_{conv} = \frac{c\Delta_{min}}{u_{max}}, \tag{2.12}$$

$$\Delta t \le \Delta t_{vis} = \frac{\Delta_{min}^2}{6\nu}, \tag{2.13}$$

where c is the Courant–Friedrichs–Lewy (CFL) number, Δt_{conv} is the time step restriction for the convection term, and Δt_{vis} is the time step restriction for the viscous term. Take simulation M_3 as an example. The CFL number c is set to 0.4, $\Delta_{min}/d_c = 0.01$, $\Delta t_{conv}\, U_\infty/d_c = 0.005$ and $\Delta t_{vis}\, U_\infty/d_c = 0.01$. Therefore, we set the time step as $\Delta t = 2 \times 10^{-3}$ to ensure computational stability. The numerical method and grid resolution selection approach are validated by comparisons with data in the literature and grid convergence tests, and the details are provided in Appendix A.

Ventilated cavitating flows are characterized by several dimensionless parameters, including: the cavitation number $\sigma_c = (p_\infty - p_c)/(0.5\rho_w U_\infty^2)$, where p_∞ and p_c are the pressure of the incoming flow and the pressure inside the cavity, respectively; the air entrainment coefficient $C_q = Q/(U_\infty d_c^2)$; the Froude number $Fr = U_\infty/\sqrt{gd_c}$, where g is the gravitational acceleration; the Reynolds number $Re = \rho_w U_\infty d_c/\mu_w$; the blockage ratio $B = d_c/D_T$, where D_T represents the hydraulic diameter of the water tunnel cross-section; and the Weber number $We = \rho_w U_\infty^2 d_c/\sigma_T$, where σ_T is the surface tension coefficient. Note that the definition of σ considers only the ventilation effect, which is consistent with previous studies, e.g. Ahn *et al.* (2017), as the vaporized liquid is negligible compared with the ventilated gas. In this study, we are interested in the scenario in which the gravitational effect is negligible; thus we set Fr to ∞. In this case, the flow field is axisymmetric, and the closure mode is RJ. Because most of the cavity has a small curvature and surface tension effects are negligible, We is set to ∞. The other dimensionless parameters are set as $C_q = 0.14$, $Re = 1000$ and $B = 1.8\%$. A relatively small Reynolds number is chosen to resolve all the turbulent eddies in the cavity by the DNS without introducing a turbulence model. Although the Reynolds number is considerably higher (10^5–10^7) in practice, the present DNS approach is still a useful research tool that provides insight into the fundamental dynamics of flow physics (Moin & Mahesh 1998). In a previous study, we found that $B = 1.8\%$ is sufficiently small to prevent blockage effects. The density ratio is set to $\rho_a/\rho_w = 0.0012$, and the dynamic viscosity ratio is set to $\mu_a/\mu_w = 0.0154$, which are realistic values for air and water.

3. Flow statistics

Although the simulation is conducted on a Cartesian grid, the data must be transformed from Cartesian coordinates, namely (x, y, z), to cylindrical coordinates, namely (r, θ, x), to analyse the flow field, which is statistically axisymmetric because $Fr = 0$, as explained in § 2.3. The transformation is performed as follows:

$$r = \sqrt{y^2 + z^2} \tag{3.1}$$

and

$$\theta = \tan^{-1}\left(\frac{z}{y}\right). \tag{3.2}$$

Finally, x remains the same in both coordinate systems.

The vector components in the cylindrical coordinate system, namely (f_r, f_θ, f_x), can be calculated according to the components in the Cartesian coordinate system, namely (f_1, f_2, f_3), as follows:

$$f_r = f_2 \cos(\theta) + f_3 \sin(\theta), \tag{3.3}$$
$$f_\theta = -f_2 \sin(\theta) + f_3 \cos(\theta), \tag{3.4}$$

and

$$f_x = f_1. \tag{3.5}$$

After the simulation reaches a fully turbulent and statistically steady state, the mean quantity of a variable f, denoted as $\bar{f}$, can be determined by averaging over both the azimuthal direction and time as

$$\bar{f}(x, r) = \frac{1}{2\pi(t_2 - t_1)}\left(\int_0^{2\pi}\int_{t_1}^{t_2} f(r, \theta, x, t)\, \mathrm{d}t\, \mathrm{d}\theta\right). \tag{3.6}$$

The integration in the azimuthal direction is performed numerically as

$$\int_0^{2\pi} f(r, \theta, x, t)\, \mathrm{d}\theta = \frac{\displaystyle\sum_{k=1}^{N_z}\sum_{j=1}^{N_y} f(x_i, y_j, z_k)\, H_r(r_{jk})}{\displaystyle\sum_{k=1}^{N_z}\sum_{j=1}^{N_y} H_r(r_{jk})}, \tag{3.7}$$

where i, j and k are the indices of discretized grid points in the x, y and z directions, and

$$H_r(r_{jk}) = \begin{cases} 1, & |r_{jk} - r| < \Delta r/2, \\ 0, & \text{other area,} \end{cases} \tag{3.8}$$

with

$$r_{jk} = \sqrt{y_j^2 + z_k^2}, \tag{3.9}$$
$$\Delta r = c(\Delta x \Delta y \Delta z)^{1/3}. \tag{3.10}$$

In the above equations, c is a constant that is set to 1.9 to ensure that $\sum_{k=1}^{N_z}\sum_{j=1}^{N_y} H_r(r_{jk}) > 0$ for all considered r values and that $\bar{f}$ is not oversmoothed.
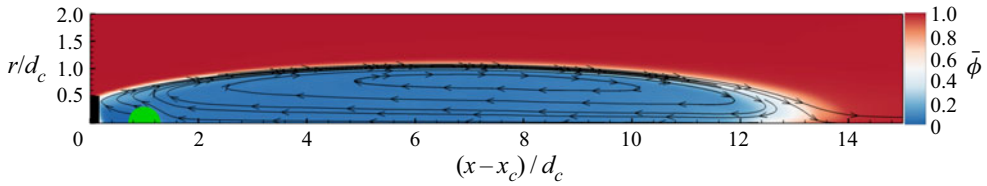
Figure 4. Contours of the mean volume fraction of water $\bar{\phi}$ and the streamlines of the mean flow field $\bar{u}$.

Statistical averaging is performed over a duration $80d_c/U_\infty$, as a fluid particle can travel through the computational domain during this period.

To consider the density difference between the water and gas phases, density-weighted averaging, which is also known as Favre averaging, is employed to analyse the results. The Favre average is expressed as

$$\tilde{f} = \frac{\overline{\rho f}}{\bar{\rho}}. \tag{3.11}$$

The fluctuations are thus defined as

$$f' = f - \bar{f} \tag{3.12}$$

and

$$f'' = f - \tilde{f}. \tag{3.13}$$

3.1. *Mean flow*

Figure 4 shows the contours of the mean volume fraction of water superimposed over the streamlines of the mean flow, which are obtained based on the time and azimuthal averages (3.6). The streamlines indicate the presence of a recirculation zone inside the cavity, in which the air travels forwards near the air–water interface but backwards near the central axis of the cavity. The mean profile of the cavity is defined by the isoline of the mean volume fraction at $\bar{\phi} = 0.5$. Figure 5 shows the contours of the mean volume fraction of water and the corresponding isolines at the closure of the cavity. The value of ϕ inside the closure region is within the range 0.2–0.8, which implies that the air and water mix violently in this region. Moreover, the contour pattern is concave near the central axis, which is due to the jet flow of the outside water. The underlying physics of this phenomenon is discussed further in the rest of § 3, as well as in §§ 4 and 5.

The streamwise and radial velocities of the air phase are defined as (Kinzel *et al.* 2009)

$$u_{x,a} = (1 - \phi)u \tag{3.14}$$

and

$$u_{r,a} = (1 - \phi)u_r, \tag{3.15}$$

where u_r is the radial velocity, which is calculated according to (3.3). They characterize the streamwise and transverse motions of air inside the cavity, as they equal the local velocities if the position is in the air phase, zero in the water phase, and $(1 - \phi)u$ and $(1 - \phi)u_r$ in grid cells with two phases.

Figures 6(*a,b*) show $\bar{u}_a$ and $\bar{u}_{r,a}$ inside the cavity. Figure 6(*a*) indicates that forward and backward motions occur inside the cavity in the red-coloured and blue-coloured areas, respectively. Figure 6(*b*) shows that compared with the streamwise velocity, the radial
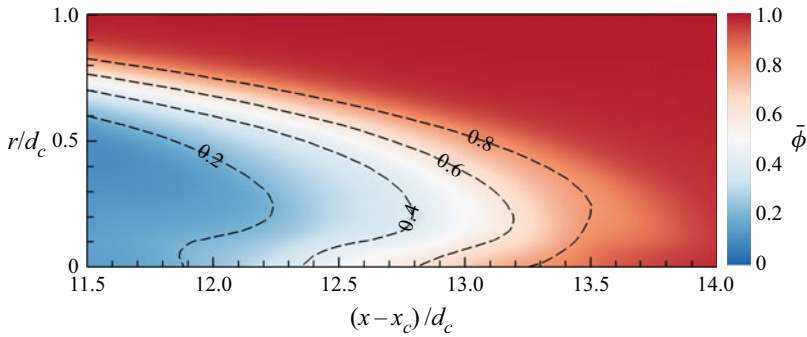
966 A20-12

Figure 5. Contours of the mean volume fraction of water, $\bar{\phi}$, and the corresponding isolines in the closure region of the cavity.

velocity of the air flow is negligible, except in the regions near the head and rear of the cavity. The $\bar{\phi} = 0.5$ contour through the red-coloured region indicates that the air moves outwards and approaches the interface at the head of the cavity before travelling inwards towards the central axis near the rear part of the cavity. These results are consistent with the flow pattern shown in figure 4.

Figures 6(*c,d*) display the contours of $\bar{u}_a$ in the middle and closure regions of the cavity. Figure 6(*c*) demonstrates that two flow structures dominate in the middle part of the cavity: the shear layer (SL), corresponding to the red-coloured contour area near the interface, and the recirculation area (RA), corresponding to the blue-coloured area near the streamwise central axis. In the SL, the flow is characterized by high local shear. In the RA, the fluid particles move backwards towards the cavitator and decelerate. Another characteristic flow structure, known as the jet layer (JL), can be observed outside the cavity near the closure region, as depicted in figure 6(*e*). One branch of the jet moves backwards and re-enters the bubble as a two-phase mixed fluid, while the other jet branch moves forwards into the wake.

The structures of the SL and RA have been discussed in previous studies (Callenaere *et al.* 2001; Spurk 2002; Kinzel *et al.* 2009). To the best of our knowledge, however, no previous studies have investigated the JL in ventilated cavitating flows. Moreover, the relationships between the SL, RA and JL and the turbulent flow in a cavity have not yet been elucidated. In the present study, the roles of these structures in turbulence generation and transport are investigated in § 4. Moreover, in § 5, their relationship with the air leakage and vortex shedding processes is discussed.

Figures 7(*a,b*) show the mean air-phase velocity profiles of the streamwise and radial components at the streamwise locations marked by the vertical lines in figure 6. Figure 7(*a*) indicates that the maximum streamwise recirculating velocity, i.e. the maximum negative $\bar{u}_a$, occurs at the central axis of the cavity. Moreover, its magnitude increases along the streamwise direction. The peak of the positive $\bar{u}_a$ occurs near the air–water interface of the cavity. This value increases until the maximum cavity radius at $(x - x_c)/d_c \sim 6$, and then decreases. Figure 7(*b*) shows that the peak value of the mean radial velocity $\bar{u}_{r,a}$ decreases before this point and then increases with the opposite sign. Furthermore, figure 7 shows that the air-phase streamwise motion dominates the radial component inside the cavity. The air-phase streamwise velocity $u_{x,a}$ is also referred to as the local rate of air entrainment in the literature (Kinzel *et al.* 2009).

Figure 8 shows the distribution of the mean cavitation number $\bar{\sigma}_c$ along the central axis. Near the closure region, $\bar{\sigma}_c$ decreases suddenly due to the increase in pressure caused by stagnation inside the JL. However, $\bar{\sigma}_c$ remains constant inside the cavity.
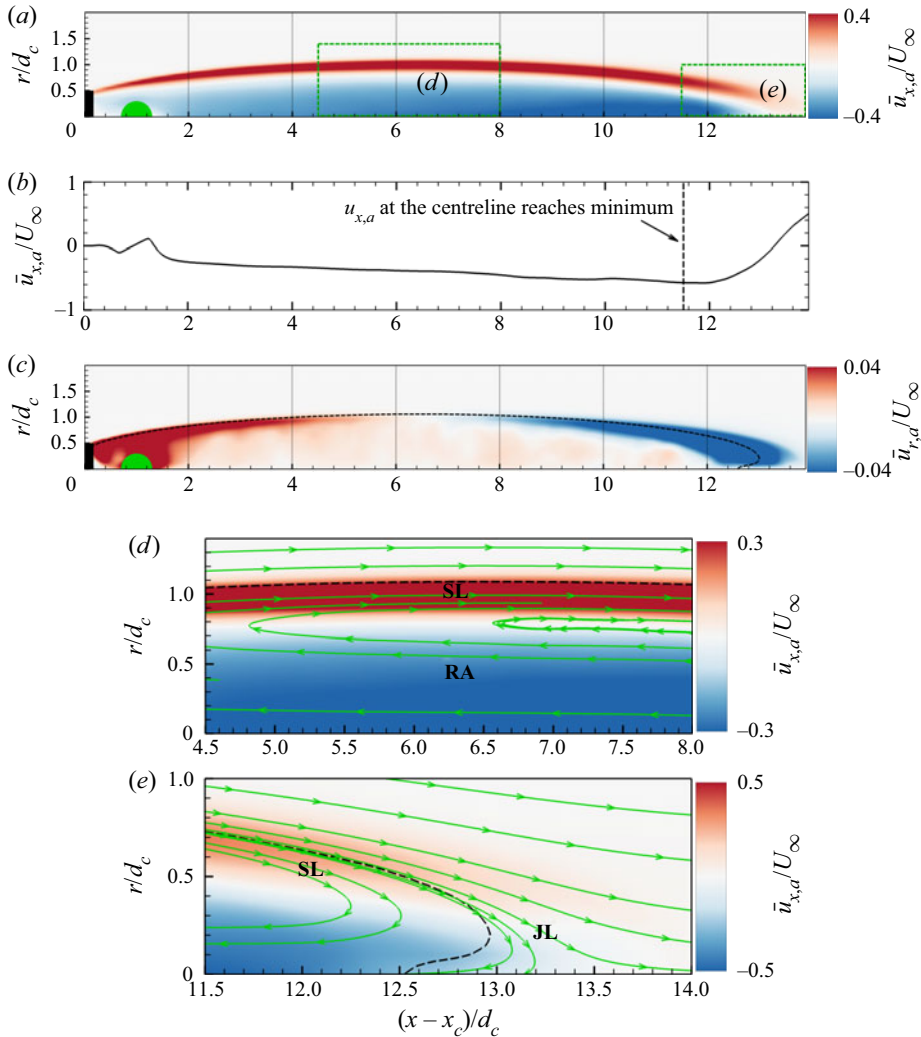
Figure 6. Contours and profile of the mean air-phase velocities: (*a*) contours of $\bar{u}_a$, (*b*) profile of $\bar{u}_a$ along the central axis, (*c*) contours of $\bar{u}_{r,a}$, (*d*) contours of $\bar{u}_a$ in the region $4.5 < (x - x_c)/d_c < 8.0$ and $0 < r/d_c < 1.4$, and (*e*) contours of $\bar{u}_a$ in the region $11.5 < (x - x_c)/d_c < 14.0$ and $0 < r/d_c < 1$. The black rectangle and green hemisphere in (*a,c*) denote the cavitator and ventilation source, respectively. The black dashed line corresponds to the isoline of $\bar{\phi} = 0.5$. The vertical solid lines in (*a,c*) indicate the locations where the cross-sectional profiles are plotted in figure 7. The green dashed rectangles correspond to the locations of (*d,e*).

3.2. *Vortex dynamics*

Because of the difficulty in obtaining measurements inside the bubble, only a few experimental studies (e.g. Yoon *et al.* 2020) on vorticity dynamics in cavities have been conducted. However, vortex dynamics are important in air leakage, air ventilation and turbulence production. In the present paper, characteristic vortex structures and the corresponding vortex dynamics are studied in the various parts of the cavity to elucidate the physical mechanisms in the cavity.

Figure 9 shows the contours of the instantaneous azimuthal vorticity ω_θ through a midplane in the computational domain. The upper blue region and lower red region
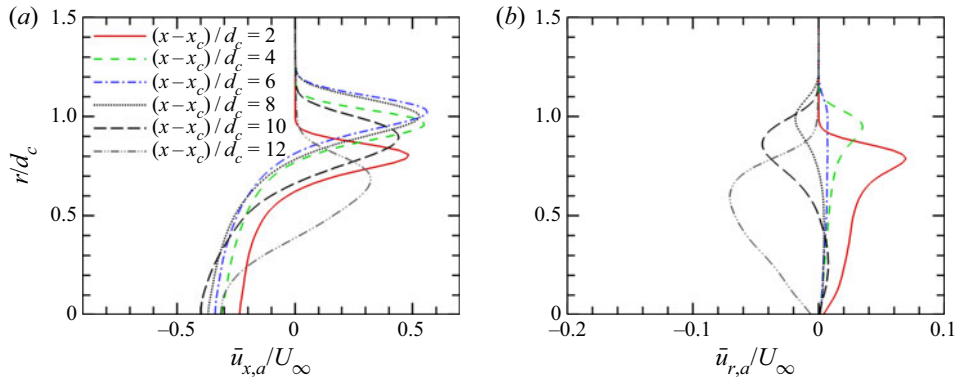
966 A20-14

Figure 7. Mean air-phase velocity profiles at different downstream locations: (*a*) streamwise velocity $\bar{u}_{x,a}$, and (*b*) radial velocity $\bar{u}_{r,a}$.
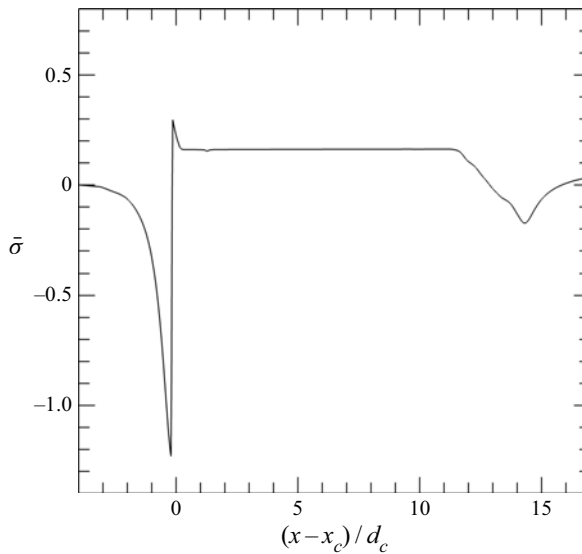

Figure 8. Variation in the mean cavitation number along the central axis in the streamwise direction.

indicate two SL structures at the front of the cavity, and the vorticity is generated mainly by the shear between the water and air phases. In the closure region, these two SL structures interact with each other and generate smaller vortex structures. Moreover, some of these small vortices leave the cavity and enter the wake flow. In the RA, i.e. the front part of the cavity, alternating red and blue vortex structures can be observed. Near-cavitator vortices were also observed experimentally by Yoon *et al.* (2020). However, these vortices were generated by a different process, namely, the interaction between the injection and reverse flows. The various mechanisms are caused by the differences in the ventilation settings between the present simulation and the experiment by Yoon *et al.* (2020). Yoon *et al.* (2020) set the direction of the injection flow towards the reversal flow, which caused interactions between the two flows, thus generating vortices. In contrast, in the present simulation, we used a spherical source to ventilate air into the cavity, which does not lead to strong interactions between the ventilated air and the reversal flow. The vortices
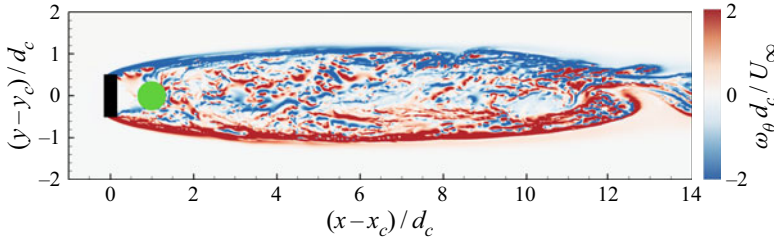
966 A20-15

Figure 9. Contours of the instantaneous vorticity component ω_θ on a midplane in the computational domain.

observed in our simulations are generated mainly in the closure region and convected backwards by the recirculating flow.

The square of the vorticity, $\zeta = (\omega_x^2 + \omega_y^2 + \omega_z^2)/2$, represents the enstrophy per unit mass. In this work, this quantity is employed to evaluate the intensity of vortex structures to study the vortex dynamics in the cavity. Specifically, the enstrophy is decomposed into two parts: $\zeta = \zeta_x + \zeta_{yz}$, where $\zeta_x = \omega_x^2/2$ is the streamwise enstrophy caused by spiral motions in the cross-sectional plane, and $\zeta_{yz} = \omega_{yz}^2 = (\omega_y^2 + \omega_z^2)/2$, which denotes the transverse enstrophy and is related mainly to shear motion in the x–r plane.

Figure 10 shows the contours of the mean enstrophy $\bar{\zeta}$ and its two components $\bar{\zeta}_x$ and $\bar{\zeta}_{yz}$. Figure 10(a) indicates that strong vortical motions occur in the SL in the front and closure regions of the cavity. Figure 10(b) shows that strong streamwise vorticity occurs only in the closure region. Moreover, figure 10(c) suggests that strong transverse vortices occur not only in the closure region of the cavity but also in the SL in the front part. In the closure region, the transverse enstrophy is larger than the streamwise enstrophy. The dominance of transverse vortical motions inside the cavity is attributed to the strong shear at the air–water interface. The strong streamwise vortical motion in the closure region suggests that the flow in this area transitions to a more three-dimensional and isotropic state due to the strong mixing between the two fluid phases in this region.

To elucidate the underlying physics of the vortex dynamics in the cavity, the mean enstrophy distributions along the radial direction are examined. Figure 11 shows the profiles of the mean enstrophy $(\bar{\zeta})$ and its two components $(\bar{\zeta}_x$ and $\bar{\zeta}_{yz})$ at different streamwise locations (see the vertical lines in figure 10) inside the cavity. The peak value of the transverse enstrophy $\bar{\zeta}_{yz}$ occurs near the interface of the cavity, where the shear effect is strong. The peak $\bar{\zeta}_{yz}$ remains approximately constant at the front (comparing $(x - x_c)/d_c = 2, 4, 6, 8, 10$) and becomes larger in the closure region $((x - x_c)/d_c = 12)$. However, the peak value of the streamwise enstrophy increases along the downstream direction until the closure region. The above variations occur because the transverse vortical motion is caused by the two-phase shear effect, which maintains a nearly constant strength in the SL in the front region, while the streamwise vortical motion is ascribed to the development of turbulence, which gradually intensifies along the streamwise direction.

To study the vortex dynamics and identify the governing mechanism during the cavity–turbulence interaction, we examine the enstrophy budget equation, which is expressed as

$$\frac{\partial(\frac{1}{2}\omega_i\omega_i)}{\partial t} + \frac{\partial(\frac{1}{2}\omega_i\omega_i u_j)}{\partial x_j} = \underbrace{\omega_i\omega_j \frac{\partial u_i}{\partial x_j}}_{W_s} + \underbrace{\frac{1}{\rho^2}\omega_i\epsilon_{ijk}\frac{\partial\rho}{\partial x_j}\frac{\partial p}{\partial x_k}}_{W_b} + \underbrace{\omega_i\epsilon_{ijk}\frac{\partial}{\partial x_j}\left(\frac{1}{\rho}\frac{\partial\sigma_{kl}}{\partial x_l}\right)}_{W_v}.$$
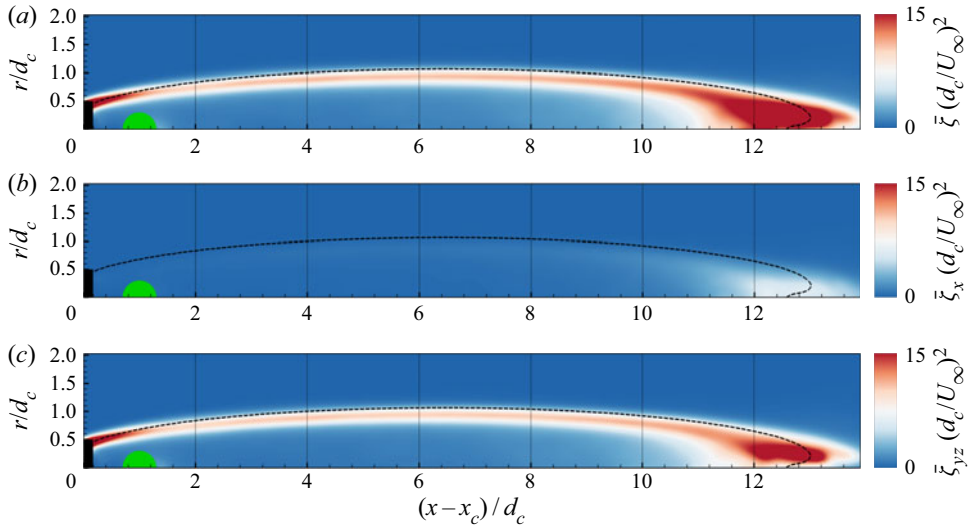
$$(3.16)$$

Figure 10. Contours of the mean enstrophy and its components: (*a*) $\bar{\zeta}$, (*b*) $\bar{\zeta}_x$, and (*c*) $\bar{\zeta}_{yz}$. The dashed line represents the isoline of $\bar{\phi} = 0.5$. The vertical solid lines indicate the locations of the cross-sectional profiles in figure 11.
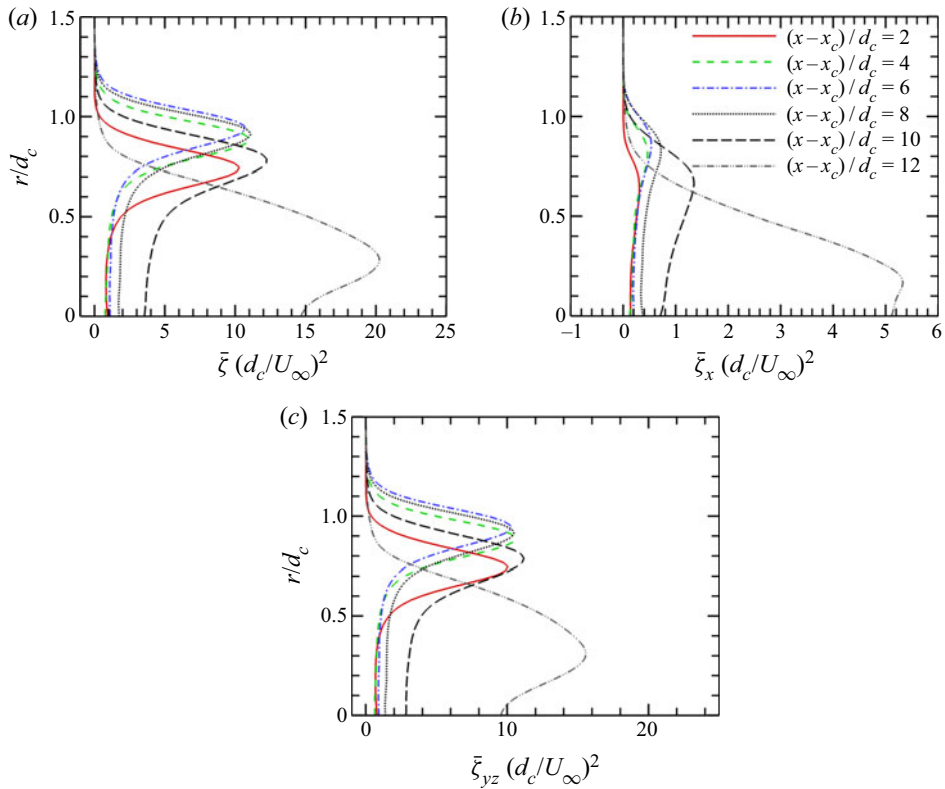

Figure 11. Profiles of the mean enstrophy and its components at different downstream locations: (*a*) $\bar{\zeta}$, (*b*) $\bar{\zeta}_x$, and (*c*) $\bar{\zeta}_{yz}$.
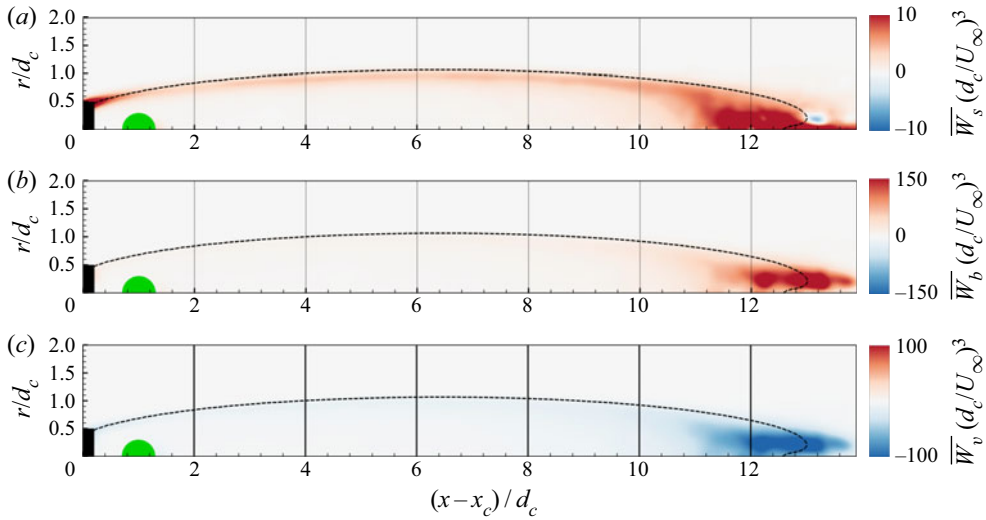
Figure 12. Contours of the mean budget terms in the enstrophy equation (3.16): (*a*) the stretching effect term $\overline{W_s}$, (*b*) the baroclinic effect term $\overline{W_b}$, and (*c*) the viscous effect term $\overline{W_v}$. The dashed line indicates the isoline of $\bar{\phi} = 0.5$. The vertical solid lines indicate the locations of the cross-sectional profiles in figure 13.

This equation is derived from the variable-density Navier–Stokes equations (2.1). The vortex dynamics is governed by three terms, namely, the stretching effect term W_s, the baroclinic effect term W_b, and the viscous effect term W_v in (3.16). These effects are displayed in figure 12. The stretching and baroclinic effects are responsible for generating enstrophy, while the viscous term dissipates enstrophy. Figure 12 shows that all three effects are weak at the front part of the cavity and strong in the closure region.

Moreover, we obtained the radial distributions of the three budget terms. Figure 13 shows the profiles of these three terms at different downstream locations. The magnitudes of the baroclinic and viscous terms are comparable and dominate the stretching term. The baroclinic effect plays an essential role in the production of enstrophy, while the baroclinic and viscous terms nearly cancel one another. In addition, the peak values of the three terms occur near the air–water interface in the cavity, and tend to increase along the downstream direction due to the increasing intense interaction between the air and water phases.

3.3. *Reynolds stresses*

Reynolds stresses play important roles in momentum transport and the interaction between turbulent fluctuations and the mean flow, which is responsible for the production of TKE. Previous studies have investigated Reynolds stress distributions in sheets and attached cavitation processes (Gopalan & Katz 2000; Iyer & Ceccio 2002). However, less is known about the Reynolds stress distribution in artificial ventilated cavitation processes. The present simulation data can be used to address this knowledge gap. In an air–water two-phase flow, Reynolds stresses are defined with a variable density. The Favre-averaged momentum equations for a variable-density flow are written as

$$\frac{\partial(\bar{\rho}\tilde{u}_i)}{\partial t} + \frac{\partial(\bar{\rho}\tilde{u}_i\tilde{u}_j)}{\partial x_j} = -\frac{\partial \bar{p}}{\partial x_i} - \frac{\partial \bar{\rho}\,\widetilde{u_i''u_j''}}{\partial x_j} + \frac{\partial \bar{\sigma}_{ij}}{\partial x_j}, \tag{3.17}$$
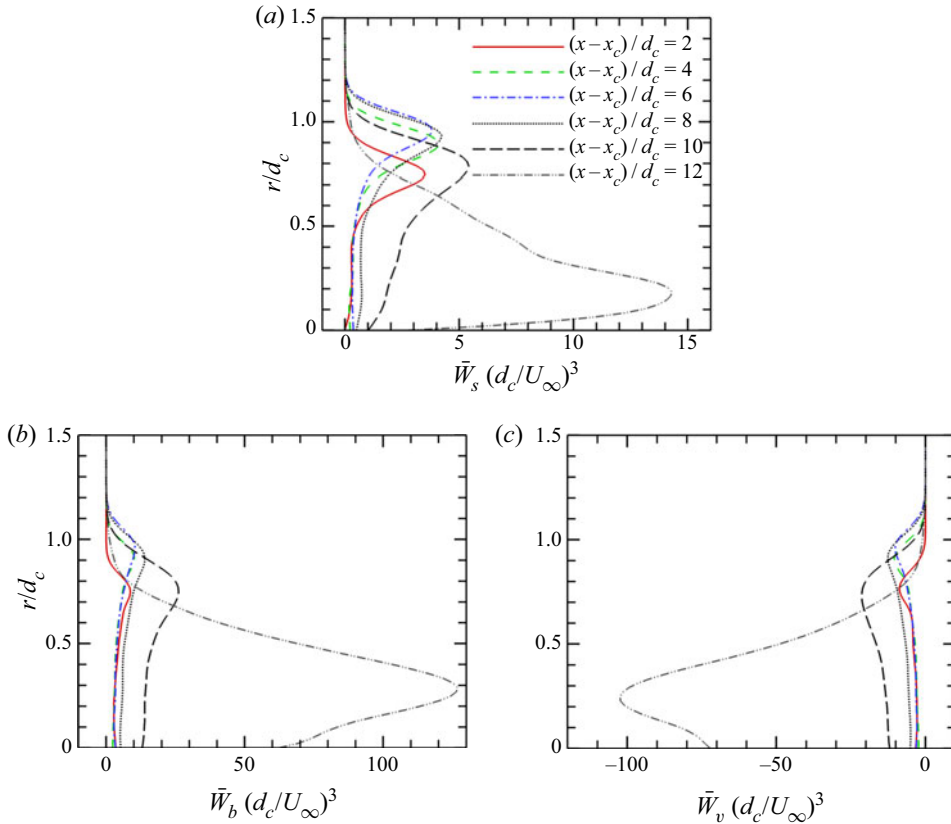
Figure 13. Profiles of the mean budget terms in the enstrophy equation (3.16) at different streamwise locations: (a) stretching effect term $\bar{W}_s$, (b) baroclinic effect term $\bar{W}_b$, and (c) viscous effect term $\bar{W}_v$.

where

$$\tau_{ij}^R = -\bar{\rho}\,\widetilde{u_i'' u_j''}, \tag{3.18}$$

is the Reynolds stress tensor. In RANS simulations, the Reynolds stresses need to be closed in terms of the mean quantities. To develop models to describe cavitating flows in the future, we study the structural characteristics and spatial distribution of the Reynolds stress. Because of the axisymmetry of the cavitating flow under investigation, the Reynolds stress components $\tau_{x\theta}^R$ and $\tau_{r\theta}^R$ are zero. Therefore, only the four independent components of the Reynolds stress tensor, namely, τ_{xx}^R, τ_{rr}^R, $\tau_{\theta\theta}^R$ and τ_{xr}^R, are considered in the discussions below.

Figure 14 shows the contours of the four components of the Reynolds stress tensor. To visualize the distributions more clearly, we also depict profiles of the Reynolds stress components at several downstream locations in figure 15. As shown in the figures, in the front part of the cavity, τ_{xx}^R is the dominant component of the Reynolds stress, while the other components are negligibly small. Figure 15(a) indicates that the maximum magnitude of τ_{xx}^R occurs at the air–water interface, where strong interactions occur between the two phases, and the peak value increases in the downstream direction. Figures 15(b,c) show that τ_{rr}^R and $\tau_{\theta\theta}^R$ are similar in the closure region of the cavity, indicating that the flow becomes more isotropic in this region. Moreover, figure 14(d) shows that τ_{xr}^R
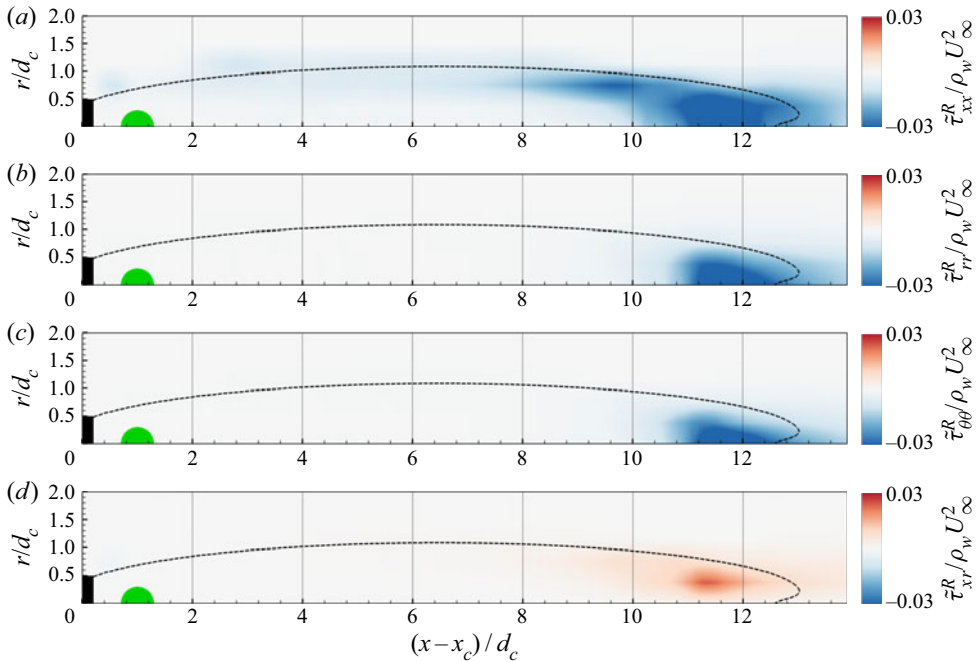
966 A20-19

Figure 14. Contours of the Reynolds stress components: (*a*) τ_{xx}^R, (*b*) τ_{rr}^R, (*c*) $\tau_{\theta\theta}^R$, and (*d*) τ_{xr}^R. The black dashed line denotes the isoline of $\bar{\phi} = 0.5$. The vertical lines indicate the locations where the cross-sectional profiles are plotted in figure 15.

is mostly positive. The quadrant analysis in Appendix B shows that the positive τ_{xr}^R component is associated with the dominant contributions of the Q_2 and Q_4 quadrants over the Q_1 and Q_3 quadrants of the Reynolds shear stress. Similarly, the peak value of τ_{xr}^R tends to occur near the two-phase interface, and increases along the streamwise direction.

In summary, the following conclusions can be drawn according to the Reynolds stress analysis. First, the peak value of the streamwise component of the Reynolds stress occurs near the air–water interface, and this component dominates the other components in most of the cavity. Second, the Reynolds stresses become stronger near the closure region, and the diagonal components are comparable, indicating that the flow becomes more turbulent and isotropic in this region.

4. Turbulence and energy budget

The TKE dynamics is particularly important in turbulence modelling. In the present multiphase flow study, based on the Favre average and the fluctuations defined in (3.11) and (3.13), the TKE is defined as

$$q = \tfrac{1}{2}u_i'' u_j''. \tag{4.1}$$

Turbulence occurs predominantly in the closure region and tends to be concentrated in the JL structure. Figure 16 plots the contours of the Favre-averaged TKE $\tilde{q}$ in this region. The TKE isolines qualitatively resemble a group of ellipses. Their centre occurs near the stagnation point in the JL, where the TKE obtains its peak value. The strong turbulence is caused by the violent mixing of air and water in this region. To further evaluate the isotropy of turbulence in the cavity, we consider the TKE fraction function (Liu & Xiao 2016),
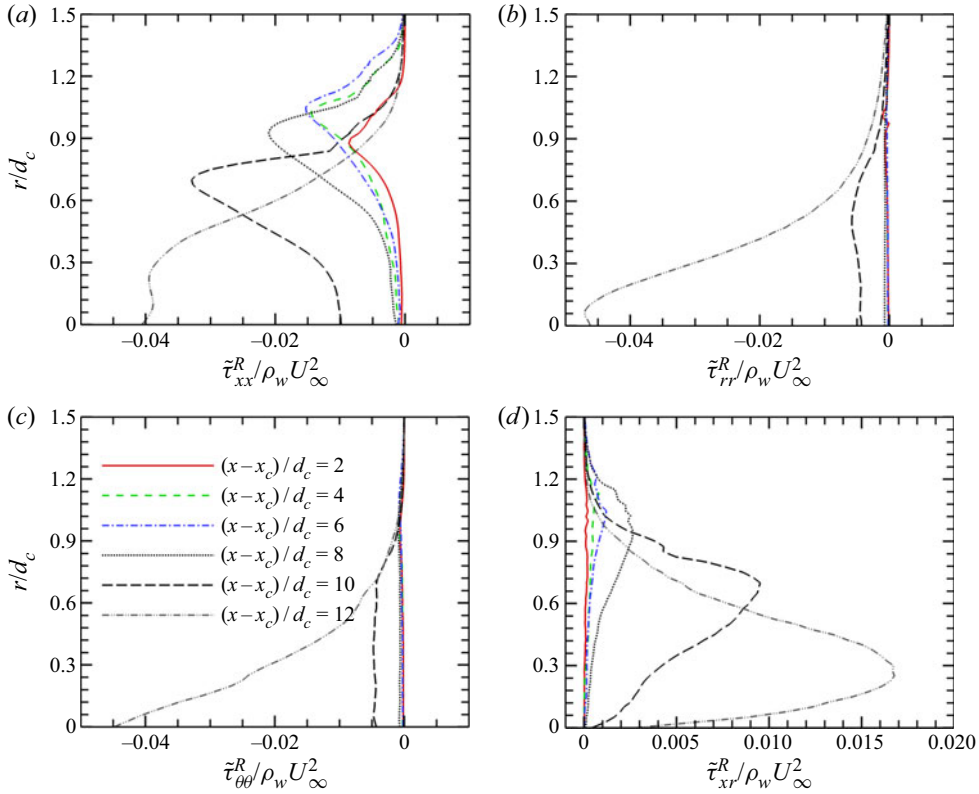
966 A20-20

Figure 15. Profiles of the Reynolds stress components at different streamwise locations: (*a*) τ_{xx}^R, (*b*) τ_{rr}^R, (*c*) $\tau_{\theta\theta}^R$, and (*d*) τ_{xr}^R.

which is expressed as

$$f_q = \frac{2\,\widetilde{u_1''u_1''}}{\widetilde{u_2''u_2''} + \widetilde{u_3''u_3''}}. \tag{4.2}$$

This fraction is twice the ratio of the TKE associated with streamwise fluctuations to that associated with transverse fluctuations. If $f_q \sim 1$, then the turbulence reaches an approximately isotropic state. Figure 17 displays the contours of f_q in the same closure region as shown in figure 16. The peaks occur near the shear layer and the stagnation point in the JL. The peak values are larger than 3.0, which indicates that the streamwise component of the TKE is considerably stronger than the transverse component of the TKE in both SL and JL.

To elucidate the mechanisms responsible for generating and transporting TKE, we examine its budget equation based on density-weighted averaging as follows:

$$0 = \underbrace{-\frac{\partial}{\partial x_j}(\bar{\rho}\tilde{q}\tilde{u}_j)}_{\Pi_c} \underbrace{-\overline{\rho u_i''u_j''}\frac{\partial \tilde{u}_i}{\partial x_j}}_{\Pi_d} \underbrace{-\frac{\partial}{\partial x_j}\left[\overline{u_j''\left(\frac{1}{2}\rho u_i''u_i''\right)}\right]}_{\Pi_{tt}} \underbrace{-\overline{u_i''\frac{\partial p}{\partial x_i}}}_{\Pi_p} + \underbrace{\frac{\partial}{\partial x_j}\left(\overline{u_i''\sigma_{ij}'}\right)}_{\Pi_{vt}} \underbrace{-\overline{\sigma_{ij}'\frac{\partial u_i''}{\partial x_j}}}_{\epsilon},$$
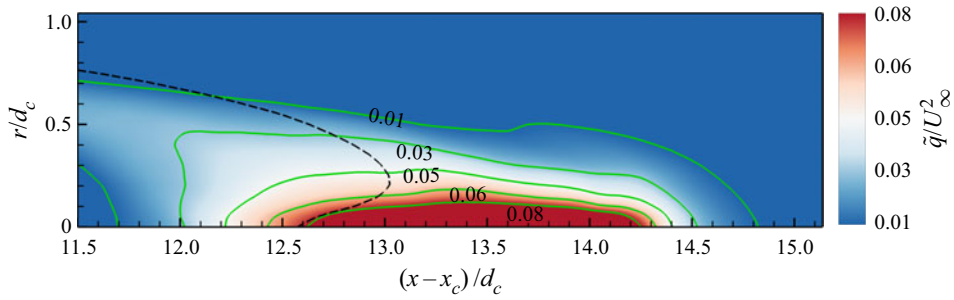
$$\tag{4.3}$$

966 A20-21

Figure 16. Contours of the Favre-averaged TKE, $\tilde{q}$. The green solid lines are the isolines of $\tilde{q}$, and the black dashed line corresponds to the isoline of $\bar{\phi} = 0.5$.
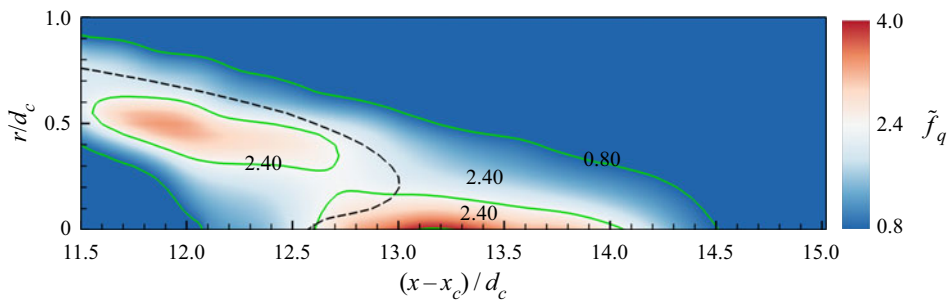

Figure 17. Contours of the TKE fraction function, f_q. The green solid lines are the isolines of f_q, and the black dashed line corresponds to the isoline of $\bar{\phi} = 0.5$.
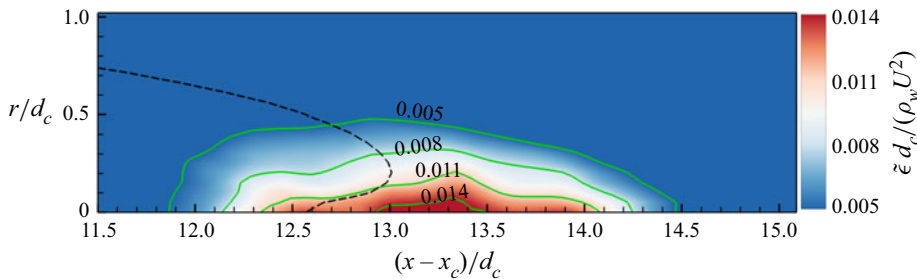

Figure 18. Contours of the viscous dissipation term ϵ. The green solid lines are the isolines of ϵ, and the black dashed line corresponds to the isoline of $\bar{\phi} = 0.5$.

where $\Pi_c = -\partial(\bar{\rho}\tilde{q}\tilde{u}_j)/\partial x_j$ is the mean flow advective transport, $\Pi_d = -\overline{\rho u_i'' u_j''}\,\partial \tilde{u}_i/\partial x_j$ is the production, $\Pi_{tt} = -\partial[\overline{u_j''(\frac{1}{2}\rho u_i'' u_i'')}]/\partial x_j$ is the turbulent transport, $\Pi_p = -\overline{u_i''\,\partial p/\partial x_i}$ is the pressure transport, $\Pi_{vt} = \partial(\overline{u_i''\sigma_{ij}'})/\partial x_j$ is the viscous transport, and $\epsilon = \overline{\sigma_{ij}'\,\partial u_i''/\partial x_j}$ is the viscous dissipation. The numerical results show that Π_{tt} and Π_{vt} are negligible (not plotted here). Therefore, in the discussions below, we focus on the remaining terms.

Figure 18 shows the contours of the dissipation term ϵ in the closure region, where the TKE is the largest (figure 16). The contour pattern is qualitatively similar to that of the TKE, especially in the JL region, as depicted in figure 16. The maximum dissipation occurs in the vicinity of the stagnation point. As is well known, ϵ is always positive and transforms TKE into internal energy.
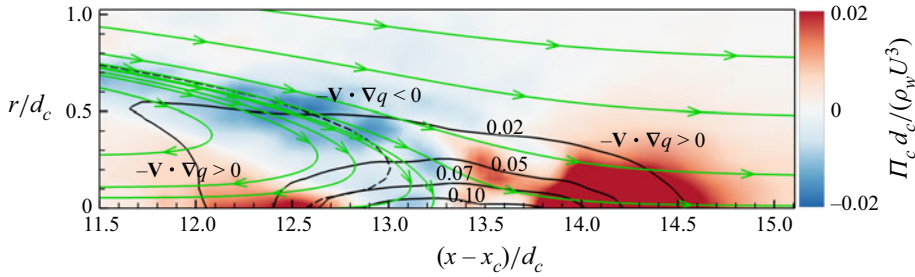
966 A20-22

Figure 19. Contours of the advective transport term Π_c. The green lines with arrows indicate the streamlines, the black dashed line corresponds to the isoline of $\bar{\phi} = 0.5$, and the black solid lines represent the TKE isolines.

Figure 19 displays the contours of the advective transport component Π_c. The blue contour in the SL indicates that energy is convected out of this region by the mean flow, and the red contour in the JL region suggests that the mean flow convects the energy into this area. This TKE transport phenomenon can be explained as follows. We can rewrite Π_c as $\Pi_c = -\bar{\rho}\tilde{u}_k \, \partial q/\partial x_k = -\boldsymbol{v} \cdot \boldsymbol{\nabla} q$. Additionally, figure 19 displays the TKE isolines. Here, $\boldsymbol{\nabla} q$ is normal to these isolines and points towards the stagnation point. The streamlines are plotted as green lines with arrows. In the SL, the mean flow moves towards the stagnation point, leading to negative Π_c ($-\boldsymbol{v} \cdot \boldsymbol{\nabla} q < 0$). Thus TKE is convected out of the SL region. However, in the JL, the mean flow moves away from the stagnation point, leading to positive Π_c ($-\boldsymbol{v} \cdot \boldsymbol{\nabla} q > 0$). Therefore, TKE is convected into the two JL branches.

The contours of the TKE production term Π_d are plotted in figure 20(a), which shows different characteristics in the SL and JL regions. The positive contour values in the red-coloured region indicate that kinetic energy is transferred from the mean flow to the turbulent flow by Π_d in the SL, while the negative contour values in the blue-coloured region indicate that energy is transferred in the reverse direction. To elucidate the physical mechanism underlying this energy transfer process, we decompose Π_d into three components:

$$\Pi_d = -\overline{\rho u_i'' u_j''} \frac{\partial \tilde{u}_i}{\partial x_j} = \Pi_{dx} + \Pi_{dt} + \Pi_{ds}, \tag{4.4}$$

where $\Pi_{dx} = -\overline{\rho u_1'' u_1''} \, \partial \tilde{u}_1/\partial x_1$ represents the production due to streamwise stretching effects, $\Pi_{dt} = -(\overline{\rho u_2'' u_2''} \, \partial \tilde{u}_2/\partial x_3 + \overline{\rho u_3'' u_3''} \, \partial \tilde{u}_3/\partial x_3)$ is the production due to the transverse motion, and $\Pi_{ds} = -(\overline{\rho u_1'' u_2''} \, (\partial \tilde{u}_1/\partial x_2 + \partial \tilde{u}_2/\partial x_1) + \overline{\rho u_3'' u_1''} \, (\partial \tilde{u}_3/\partial x_1 + \partial \tilde{u}_1/\partial x_3))$ is the production due to shear effects. Figure 20(b) shows that Π_{dx} is negative in both the SL and JL. Figure 20(c) indicates that Π_{dt} is positive and concentrated in the JL. Figure 20(d) shows that Π_{ds} is mainly positive and concentrated in the SL. Note that Π_d is positive in the SL and negative in the JL. Therefore, Π_{ds} dominates in the SL, while Π_{dx} dominates in the JL. To further assess the relative importance of the above terms, we calculate the fraction functions of the magnitudes of different terms as

$$f_{dx} = |\Pi_{dx}|/(|\Pi_{dx}| + |\Pi_{dt}| + |\Pi_{ds}|), \tag{4.5}$$

$$f_{dt} = |\Pi_{dt}|/(|\Pi_{dx}| + |\Pi_{dt}| + |\Pi_{ds}|), \tag{4.6}$$

and

$$f_{ds} = |\Pi_{ds}|/(|\Pi_{dx}| + |\Pi_{dt}| + |\Pi_{ds}|). \tag{4.7}$$
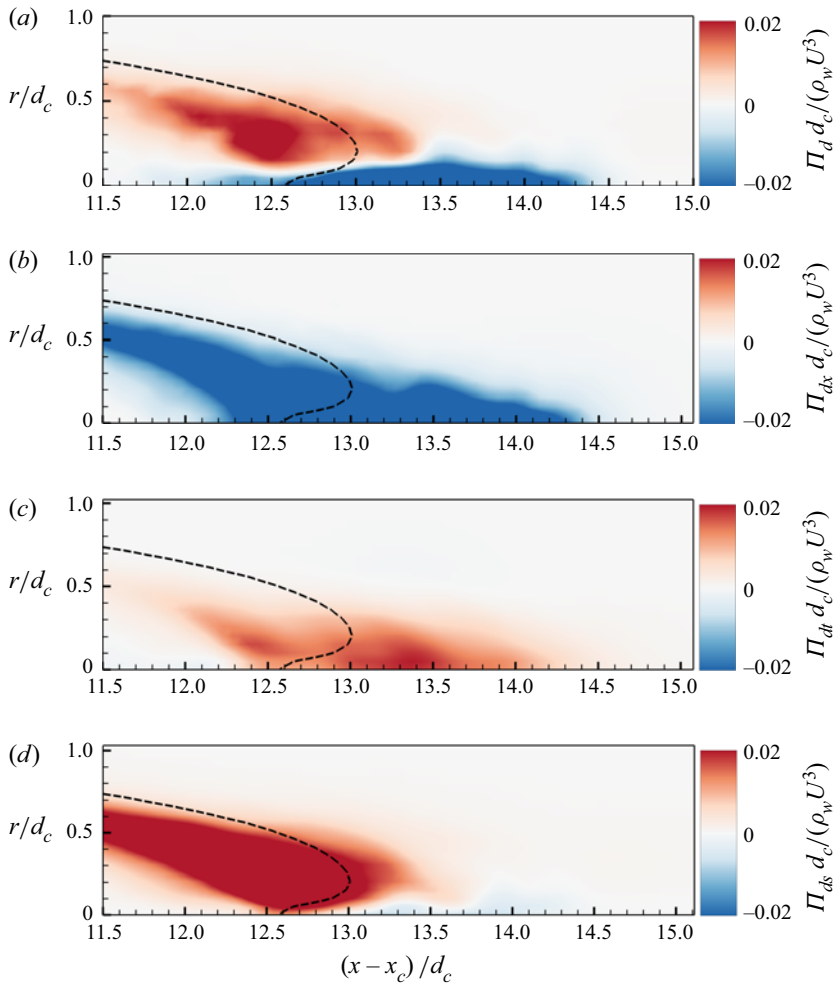
Figure 20. Contours of the TKE production term and its components: (*a*) Π_d, (*b*) Π_{dx}, (*c*) Π_{dt}, and (*d*) Π_{ds}. The black dashed line represents the isoline of $\bar{\phi} = 0.5$.

In both the SL and JL, compared with f_{dx} and f_{ds}, f_{dt} is negligible (not plotted). The contours of f_{dx} and f_{ds} are depicted in figures 21(*a,b*): f_{dx} is concentrated in the JL, while f_{ds} dominates in the SL. These results can be explained by the distributions of the Reynolds stress and mean strain rate in the closure region of the cavity. In the SL, the shear effect leads to a positive and strong $\partial \tilde{u}_x / \partial r$. Moreover, the Reynolds stress τ_{xr}^R is positive and non-negligible. Hence the TKE production rate is dominated by the positive Π_{ds} component. However, in the two JL branches, the jet flow increases the stretch-strain rate components, i.e. the jet flow generates negative $\partial \tilde{u}_r / \partial r$ and positive $\partial \tilde{u}_x / \partial x$ components with large magnitudes.

Note that the streamwise Reynolds stress dominates in the JL (see figure 17). Consequently, the TKE production rate is dominated by the negative Π_{dx} component in the JL because of the negative τ_{xx}^R and positive $\partial \tilde{u}_x / \partial x$.
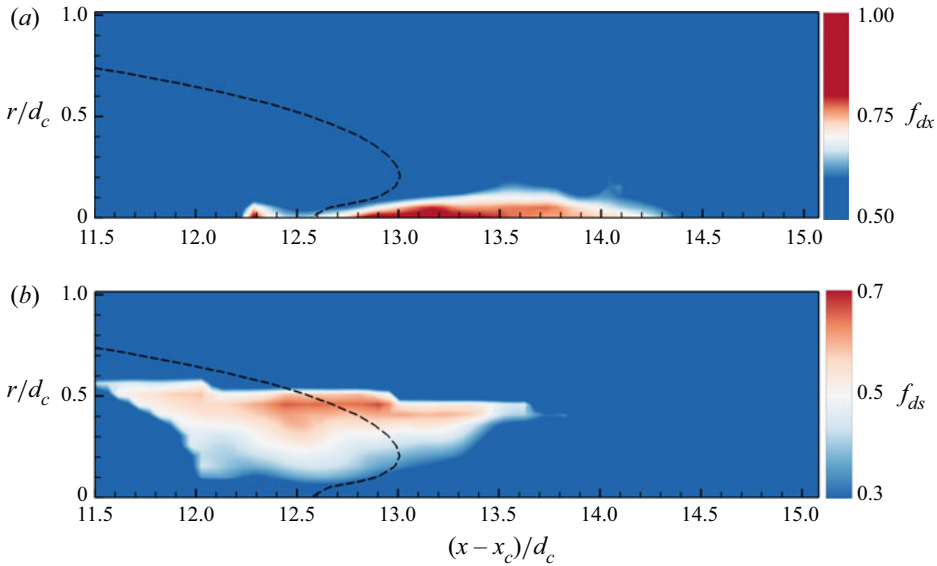
Figure 21. Contours of the fraction functions of the components of Π_d: (a) f_{dx}, and (b) f_{ds}. The black dashed line represents the isoline of $\bar{\phi} = 0.5$.

The TKE pressure transport term can be decomposed into three parts:

$$\Pi_p = -\overline{u_k'' \frac{\partial p}{\partial x_k}} = \Pi_{pm} + \Pi_{pt} + \Pi_{pd}, \tag{4.8}$$

where $\Pi_{pm} = -\overline{u_k''} \, \partial \bar{p}/\partial x_k$ is the transport due to the mean pressure gradient, $\Pi_{pt} = -\overline{\partial p' u_k''}/\partial x_k$ is the transport due to the pressure–velocity fluctuation correlation, and $\Pi_{pd} = \overline{p' \, \partial u_k''/\partial x_k}$ is the transport due to the dilatation effect. Note that Π_{pd} decreases because of the incompressibility of the two phases. The contours of Π_{pm} and Π_{pt} are displayed in figures 22 (a,b). The figure shows that Π_{pm} is positive in both the SL and JL, which enhances the TKE in the closure region of the cavity. On the other hand, Π_{pt} is largely negative in the SL and tends to transport TKE from the SL region to the JL region.

To summarize § 4, figure 23 illustrates the energy transfer processes among the turbulent flows in the SL and JL regions and the mean flow. The aforementioned results show that the SL and JL structures have distinct characteristics during TKE generation and transport. In the SL, the TKE is increased by the production term due to the shear effect term Π_{ds}, while in the JL structure, the TKE decreases due to the streamwise stretching effect term Π_{dx}. The pressure transport term Π_{pm} tends to enhance the TKE in both the JL and SL. Moreover, the mean flow advective transport term Π_c and pressure transport term Π_{pt} are conducive to transporting TKE from the SL to the JL.

5. Air leakage and vortex shedding

In ventilated cavitation, some air escapes from the cavity through the closure part, where violent flow mixing between water and air occurs. Wu *et al.* (2019) conducted experiments and used particle image velocimetry to study quantitatively the gas leakage process that occurred in the RJ and TV closure modes. Moreover, they discussed the variation in gas leakage during the transition between the RJ and TV modes. Their results indicated that
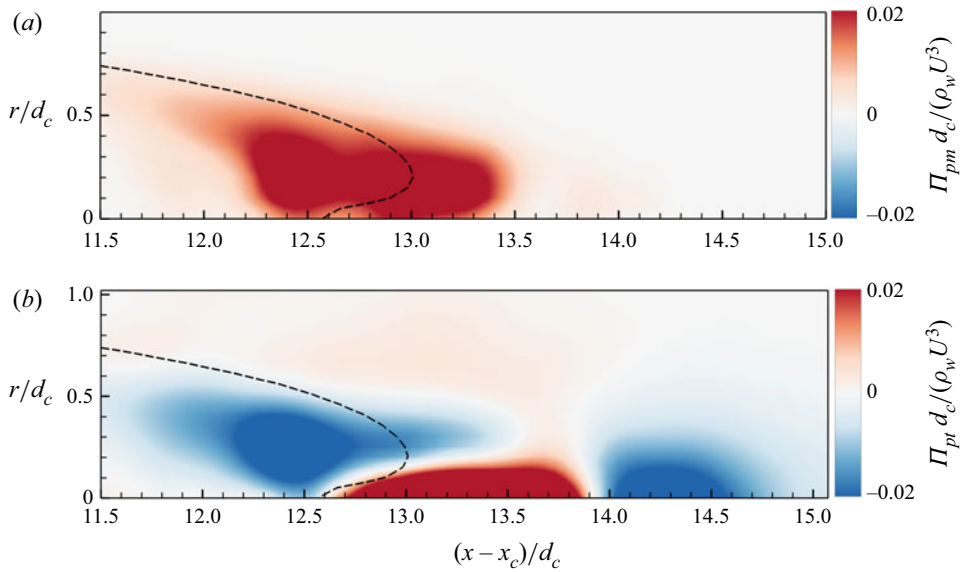
Figure 22. Contours of the pressure transport terms: (*a*) Π_{pm}, and (*b*) Π_{pt}. The black dashed line denotes the isoline of $\bar{\phi} = 0.5$.
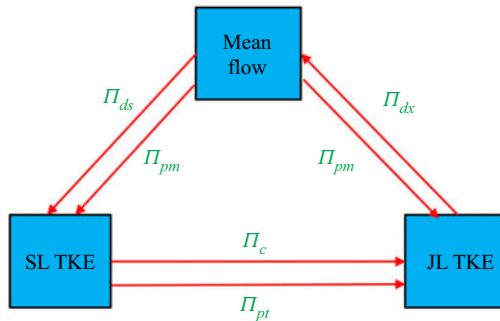

Figure 23. Schematic of the energy transport among the mean flow, SL turbulent flow and JL turbulent flow.

gas leakage occurs due to interactions between the internal and external flows. According to the present simulation results, we made several observations to elucidate the flow characteristics and dynamics in the RJ closure region of the cavity.

First, the simulation data indicate that the air leakage process in the closure region has a one-to-one correspondence with the vortex shedding process, as shown by the instantaneous visualization of the flow. Previous studies (Shao *et al.* 2017; Karn, Arndt & Hong 2016) have shown that the RJ mode leaks gas via toroidal-like vortices. However, these works did not connect the gas leakage to the vortex shedding process. Figures 24(*a,b*) plot the isosurfaces of the VOF function $\phi = 0.5$ and the second invariant of the strain rate tensor $Q = 2$, with the former coloured according to the magnitude of the pressure, and the latter coloured according to the magnitude of ϕ. The leakage air–water interface exhibits the same pattern as the vortex structures characterized by Q (Haller 2005).

Furthermore, only a few previous laboratory studies (Karn *et al.* 2016; Wu *et al.* 2019) identified the location where the air pockets leave the cavity and the associated vortex shedding. From our simulation result, flow visualization shows that air leakage
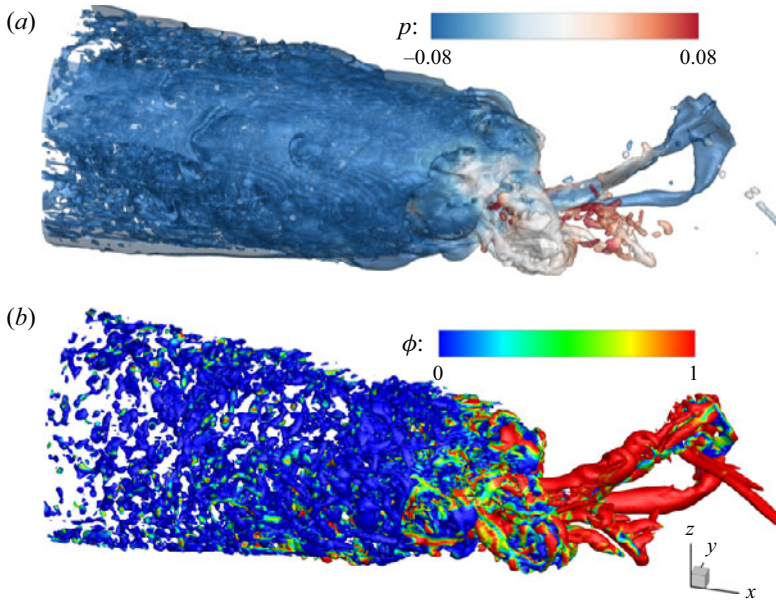
966 A20-26

Figure 24. Instantaneous structures of air leakage and vortex shedding in the closure region of the cavity. (*a*) Isosurface of $\phi = 0.5$, which is coloured according to the magnitude of the pressure. (*b*) Isosurface of the second invariant of the strain rate tensor ($Q = 2$), which is coloured according to the magnitude of ϕ.

and vortex shedding occur within the JL structure in the closure region. The colours in figure 24(*a*) illustrate the pressure distribution on the surface of the cavitation bubble. The disconnection and breakup of the leaked air flow structures from the body of the cavity occur near the high-pressure region, which corresponds to the stagnant region inside the JL structure. The vortex structures in figure 24(*b*) are coloured according to the value of ϕ on the isosurface. The results indicate that vortex tubes and rings occur in the violent air–water mixing region, i.e. the JL region.

Moreover, we observe that the air leakage and vortex shedding processes in the closure region of the cavity are not random, and these processes exhibit semi-periodic patterns with intrinsic characteristic frequencies. Few previous experimental works have investigated the spectra and oscillation patterns of the closure modes due to measurement limitations. Jiang, Shao & Hong (2018) conducted a spectral analysis of the cavity length but did not find a dominant oscillation frequency. In the present study, our three-dimensional simulation results illustrate more details about the oscillations within the different structures in the closure mode.

To investigate the relationship between the vortex shedding and air leakage processes, we employ a temporal Fourier transform to obtain the frequency spectra of the radial velocity $E(u_r)$ and the VOF function $E(\Phi)$. The results for $10 < (x - x_c)/d_c < 15$ along the central axis are shown in figure 25. Figures 25(*a*) and 25(*b*) both indicate a significant characteristic frequency, namely $St \approx 0.1$, where the spectra reach their local peaks, indicating that the air leakage and vortex shedding processes share the same characteristic frequency. Moreover, the spectra are more concentrated in the $12.5 < (x - x_c)/d_c < 14$ region, where the turbulent mixing between the air and water is violent, which contributes to the strong turbulence within this region.

The air leakage frequency can also be quantified by defining the total air volume as a function of time in a fixed control volume (CV) bounded by $12.5 < (x - x_c)/d_c < 14$ and
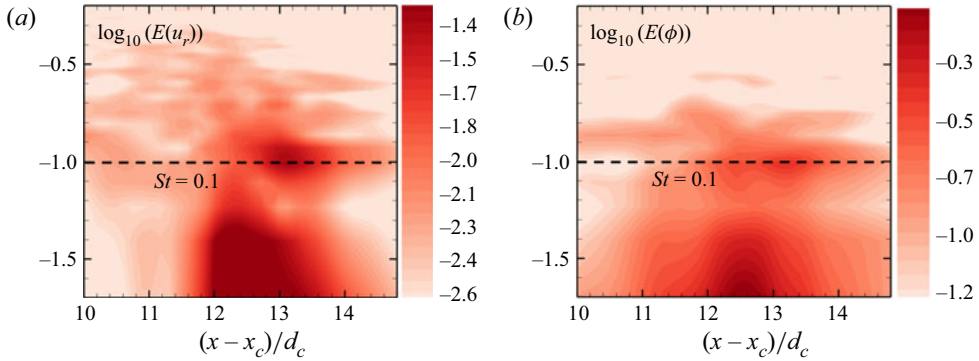
Figure 25. Frequency spectra of the radial velocity u_r and VOF function ϕ along the central axis: (a) $\log_{10}(E(u_r))$, and (b) $\log_{10}(E(\phi))$.

$r/d_c < 0.8$. The total volume of air $V_a(t)$ in the CV is expressed as

$$V_a(t) = \int_{\boldsymbol{x} \in CV} \phi(\boldsymbol{x}, t) \, \mathrm{d}\boldsymbol{x}. \tag{5.1}$$

We then define the following normalized autocorrelation function for V_a:

$$R_V(\Delta t) = \frac{\displaystyle\int_0^T V_a(t) \, V_a(t + \Delta t) \, \mathrm{d}t}{\displaystyle\int_0^T V_a(t) \, V_a(t) \, \mathrm{d}t}. \tag{5.2}$$

Figure 26 shows $R_V(\Delta t)$ versus the time interval Δt, normalized by d_c and U_∞. A peak occurs at $\Delta t = 11.1 d_c / U_\infty$, which corresponds to the Strouhal number $St = 0.09$. This value is close to the peak in the frequency spectra of the radial velocity and VOF function (figure 25). In other words, the air leakage and vortex shedding processes occur at the same frequency, and the two processes are strongly correlated in the closure region in ventilated cavitating flows.

In summary, figures 24–26 demonstrate several properties about the air leakage and vortex shedding processes. First, the generation of vortex structures is associated with the leakage of air bubbles. Both processes occur in the stagnant high-pressure region with violent turbulent mixing between the air and water phases. Second, the vortex shedding in the closure region shows a semi-periodic pattern, and an intrinsic characteristic frequency can be observed in the energy spectra. Third, the air leakage and vortex shedding processes share the same characteristic frequency. Based on the above results, we summarize the air leakage and vortex shedding processes in the closure region of the cavity in the sketch in figure 27. The underlying mechanism can be described as follows. Air is convected forwards through the SL and then terminates, which is accompanied by the generation of vorticity in the SL, as shown by Part 1 in the figure. Due to the constant ventilation from the front part of the cavity, the air cannot remain in the end of the SL region and thus moves into the JL in the closure region, where the air and water are fully mixed, as shown by Part 2 in figure 27. Finally, the air leaks and exits the cavity, generating complex vortex structures that are convected downstream, as depicted in Part 3.
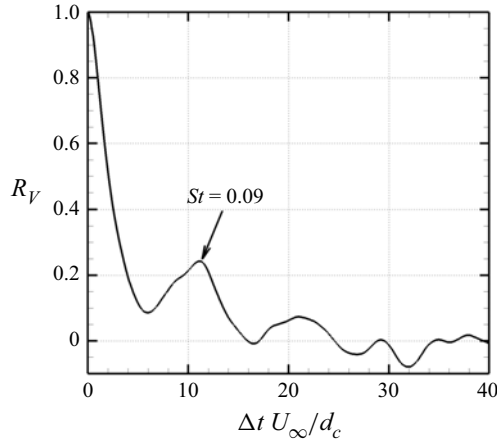
Figure 26. Normalized autocorrelation function of the bubble volume in the region $12.5 < (x - x_c)/d_c < 14$, $r/d_c < 0.8$.
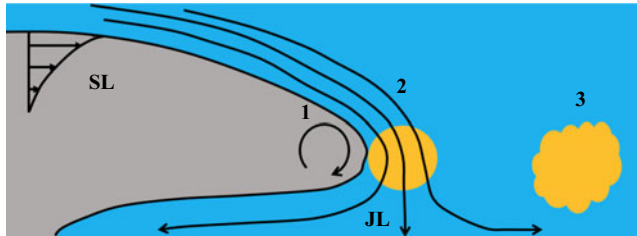

Figure 27. Schematic of the air leakage and vortex shedding processes. Part 1: vorticity is generated in the SL and convected to the end of the cavity. Part 2: the air in the JL in the cavity continues to convect. Part 3: the air leaks accompanied by the formation of complex large-scale vortex structures.

6. Spectral proper orthogonal decomposition analysis of coherent structures

In this section, we employ the SPOD method (Towne *et al.* 2018) to extract and analyse the coherent structures near the closure region of the ventilated cavitating flow. To perform the SPOD analysis, N_s snapshots of the flow field q acquired at constant time intervals are decomposed into a set of blocks along the temporal direction as $Q = [q^{(1)}, q^{(2)}, \ldots, q^{(i)}, \ldots, q^{(N_{freq})}]$, where i is the index of the block, $q = [u_x, u_r, u_\theta]$ is the vector of the velocity components in cylindrical coordinates, and N_{freq} is the number of snapshots in each block (Nidhan *et al.* 2022). To improve our spectral analysis, we include N_{ovl} overlapping snapshots between neighbouring blocks, following the treatment in Schmidt & Colonius (2020). Therefore, the total number of blocks after this decomposition can be calculated as

$$N_{blk} = \frac{N_s - N_{ovl}}{N_{freq} - N_{ovl}}. \tag{6.1}$$

Then a temporal Fourier transform is performed in each block to obtain the projections in the frequency domain as

$$q^{(j)}(x, r, \theta, t) = \Sigma_\omega \hat{q}_\omega^{(j)}(x, r, \theta) e^{i\omega t}, \tag{6.2}$$

where i is the imaginary unit, and $\omega = 2\pi St$ is the angular frequency, which is calculated according to the Strouhal number $St = d_c f / U_\infty$. The obtained ensemble of N_{blk} blocks
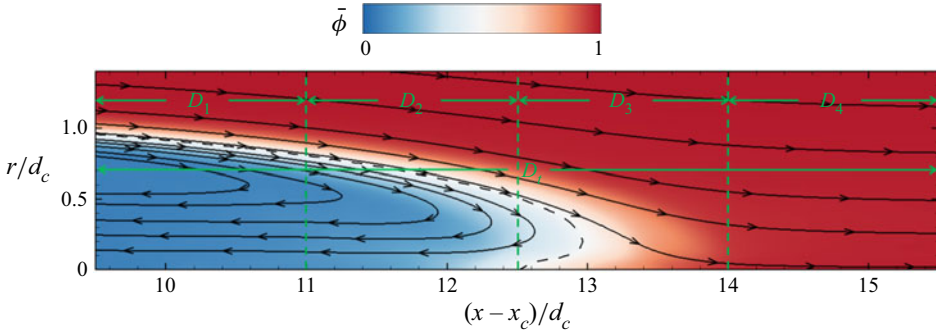
966 A20-29

Figure 28. Contours of the mean volume fraction of water $\bar{\phi}$ and the streamlines of the mean flow field near the closure region. The four subdomains D_1, D_2, D_3 and D_4, and the whole domain D_t, for the SPOD analyses are shown. The black dashed line is the isoline of $\bar{\phi} = 0.5$.

with frequency ω is denoted as $Q_\omega = [\hat{q}_\omega^{(1)}, \hat{q}_\omega^{(2)}, \ldots, \hat{q}_\omega^{(N_{freq})}]$. After the Fourier transform, we calculate the SPOD eigenvalues and eigenvectors corresponding to the frequency ω via eigenvalue decomposition as

$$\hat{Q}_\omega^* W \hat{Q}_\omega \Psi_\omega = \Psi_\omega \Lambda_\omega, \tag{6.3}$$

where W is a weighting matrix, and $\Lambda_\omega = \mathrm{diag}(\lambda_\omega^{(1)}, \lambda_\omega^{(2)}, \ldots, \lambda_\omega^{(N_{blk})})$ is a diagonal matrix containing the eigenvalues ranked according to decreasing energy from $j = 1$ to N_{blk}. The jth SPOD mode $\Phi_\omega^{(j)}$ is computed as

$$\hat{\Phi}_\omega = \hat{Q}_\omega \Psi_\omega (\Lambda_\omega)^{-1/2}. \tag{6.4}$$

An energy-based inner product is employed to compute the eigenvalues and eigenvectors by defining the weight matrix W as a trapezoidal integration matrix. Thus the norm can be calculated as

$$\hat{Q}_\omega^* W \hat{Q}_\omega = \int \int \int_D \hat{Q}_\omega^* \, \mathrm{diag}(1, 1, 1) \, \hat{Q}_\omega r \, \mathrm{d}r \, \mathrm{d}x \, \mathrm{d}\theta, \tag{6.5}$$

where D is the domain of interest. More details on the SPOD formulation can be found in Towne *et al.* (2018) and Nidhan *et al.* (2022).

For the SPOD analysis in the present work, we use $N_s = 4096$ consecutive snapshots of the plane at $z = 0$ spanning $9.5 < (x - x_c)/d_c < 15.5$ and $0 < (y - 0.5L_y)/d_c < 1.3$, which includes the closure region of the ventilated cavity. The time interval for the sampled snapshots is $\Delta t d_c/U_\infty = 0.1$. We select the number of frequencies as $N_{freq} = 512$, and implement a 50 % overlap between blocks, i.e. $N_{ovl} = 256$, to balance improved spectral convergence with reduced spectral entanglement between each window in the Fourier transform. Each data block is multiplied by a Hamming window function before the Fourier transform to effectively reduce errors due to spectral leakage (Schmidt & Colonius 2020). To study the variation in the eigenspectral features at different locations, we perform SPOD analyses in four consecutive domains, D_1, D_2, D_3 and D_4, which are shown in figure 28.
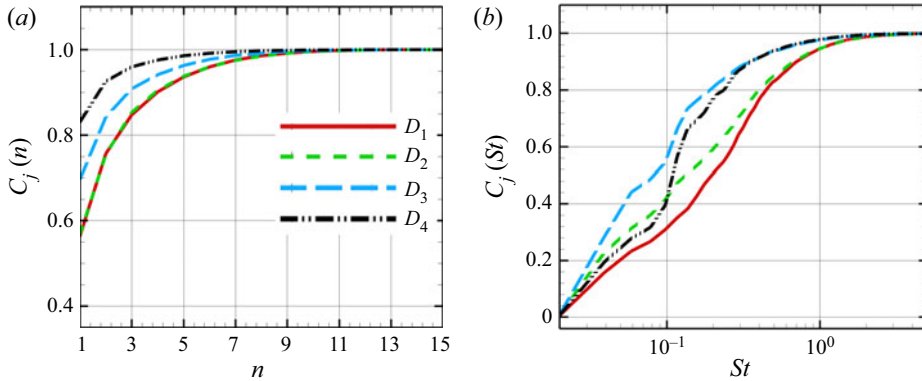
Figure 29. Cumulative fraction of energy in different domains, C_j: (*a*) as a function of the modal index n; and (*b*) as a function of St. The plots are shown for the four considered domains, namely D_1, D_2, D_3 and D_4.

We start our analysis of the SPOD modes by studying their relative contributions to the fluctuation energy. Figure 29(*a*) shows the cumulative fraction of energy, $C_j(n)$, as a function of the SPOD modal index n in the four downstream domains D_1, D_2, D_3 and D_4, which is computed as

$$C_j(n) = \frac{\sum_{i=1}^{n} \sum_{s=St_{min}}^{St_{max}} \lambda_s^{(i)}(D_j)}{\sum_{i=1}^{N_{blk}} \sum_{s=St_{min}}^{St_{max}} \lambda_s^{(i)}(D_j)}. \tag{6.6}$$

A comparison of the curves among the different subdomains indicates that the relative energies contributed by the leading SPOD modes increase with the downstream distance. In addition, we observe that the curves for D_1 and D_2 essentially collapse onto a single curve, whereas the curves for D_2 and D_3 differ considerably, indicating that a transition occurs between D_2 and D_3. This result is consistent with our observation in figure 25 that D_3 contains the region where the air and water mix violently and the turbulence intensity is strong. Moreover, figure 29(*a*) demonstrates that the first SPOD mode contributes a significant fraction of the total energy, contributing approximately 60 % of the energy in D_1 and D_2, and approximately 70 % and 80 % of the energy in D_3 and D_4, respectively. These results indicate low-rank behaviours, which are used to describe scenarios in which the physical mechanism associated with the leading mode dominates (Schmidt *et al.* 2018).

The SPOD analyses have shown that low-rank behaviours can be observed in various flow dynamics, including turbulent stratified wakes (Nidhan *et al.* 2022), jet turbulence (Schmidt *et al.* 2018) and turbulent premixed flames (Brouzet *et al.* 2020). In the present study, the low-rank behaviour is prevalent near the closure region of the ventilated cavitating flow, and the results in figure 29(*a*) show that the low-rank behaviour becomes stronger with increasing downstream distance in the closure region.

The cumulative fraction of energy contributed by SPOD modes as a function of dimensionless frequencies, measured by St, is computed as

$$C_j(St) = \frac{\displaystyle\sum_{s=St_{min}}^{St} \sum_{i=1}^{N_{blk}} \lambda_s^{(i)}(D_j)}{\displaystyle\sum_{s=St_{min}}^{St_{max}} \sum_{i=1}^{N_{blk}} \lambda_s^{(i)}(D_j)}, \tag{6.7}$$

which is plotted in figure 29(*b*). The figure shows that in the downstream direction, $C_j(St)$ in the range $0 < St < 0.4$ first increases (D_1 to D_3) and then decreases (D_3 to D_4). However, $C_j(St)$ in the higher frequency range ($0.4 < St$) increases monotonically. This result indicates an energy redistribution in the frequency domain in the closure region, which is caused by the interaction between the SL and JL structures, as discussed in § 5. Additionally, figure 29(*b*) shows that the curves have inflection points near the characteristic frequency $St = 0.1$, which is more pronounced for D_3 and D_4. This result indicates that the SPOD modes oscillating around the characteristic frequency contribute a significant amount of energy.

Next, we discuss the SPOD eigenspectra. Figure 30 shows the SPOD eigenspectra $\lambda^{(i)}$ in the different downstream domains. The red shades in the figure indicate significant differences between the first and second modes in each domain. This result is consistent with our previous observation of low-rank behaviour. Moreover, the differences tend to be larger in the low-frequency range, indicating that the low-rank behaviour is more pronounced at lower frequencies. In addition, the figure shows a distinct spectral peak at approximately $St = 0.1$, which can also be observed in our other spectral results (figures 25 and 26). This characteristic frequency is correlated with the oscillatory dynamics of the coherent structure at this frequency. Moreover, by comparing figures 30(*c*,*d*) and 30(*a*,*b*), we find that the distinct spectral peaks in D_3 and D_4 are higher than those in D_1 and D_2. This difference occurs because the turbulence intensity is stronger in D_3 and D_4 than in D_1 and D_2.

Based on the above analyses, we summarize the implications from figures 29 and 30 as follows. (i) The relative contributions by the leading SPOD modes increase with increasing downstream distance. (ii) The SPOD modes show low-rank behaviours. The first mode dominates and is more pronounced in the low-frequency range. (iii) A distinct spectral peak exists in the SPOD eigenspectrum.

To analyse the dominant coherent structures oscillating at different frequencies near the closure region, we study the real part of the first SPOD mode for the radial velocity $\Phi_r^{(1)}(x, r, St)$, which was obtained by performing the SPOD analysis in the whole domain D_t, and is plotted in figure 28. The results in figure 31 are consistent with those obtained by phase matching the modes obtained in the four subdomains, and provide a global view. According to the analysis in § 3, two characteristic structures can be observed near the cavity closure, i.e. the SL, where the shearing effect dominates, and the JL, where the stretching effect caused by the strong pressure gradient dominates. According to figure 31, we can identify finer coherent structures located near the SL and JL. Figure 31(*a*) shows the first SPOD mode at the characteristic frequency $St = 0.1$. Near the right branch of the JL, we observe a wavepacket spanning from the end of the SL to the wake region. A comparison of figures 31(*a*)–31(*d*) shows that the spatial wavelength and span of this wavepacket decrease with increasing St. Figures 31(*c*) and 31(*d*) show another wavepacket located parallel to the first structure and closer to the central axis. Combined with
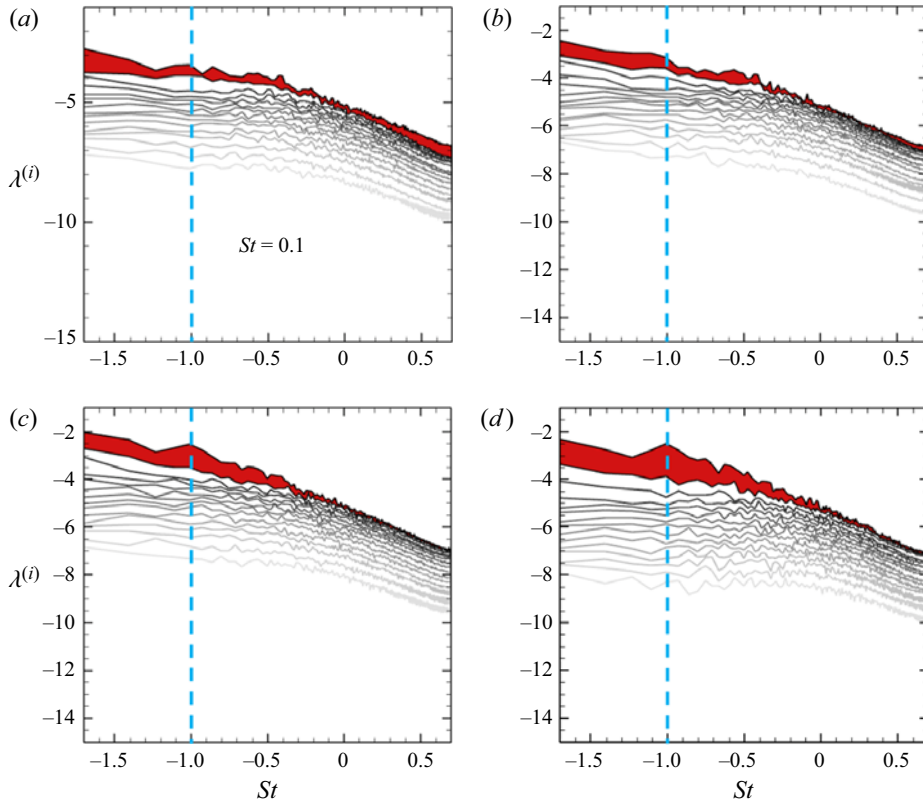
Figure 30. SPOD eigenspectra obtained in the four domains: (*a*) D_1, (*b*) D_2, (*c*) D_3, and (*d*) D_4. The dark to light colours correspond to the increasing model index i in $\lambda^{(i)}$. The red shade between $\lambda^{(1)}$ and $\lambda^{(2)}$ indicates their difference.

the visualization of the Q-criterion in figure 24, we can infer that the outer and inner wavepackets are both associated with the vortex shedding dynamics near the closure region. However, the outer wavepacket is associated with the shedding of larger vortical structures from the end of the SL, which include mainly elongated and tilting toroidal vortices, whereas the inner wavepacket is associated with the smaller and more isotropic vortical structures shed from the central part of the closure region ($r/d_c < 0.5$). We refer to these two coherent structures as JL_{out} and JL_{in}, respectively, as indicated in figure 31(*c*). Note that at $St = 0.1$, JL_{out} dominates over JL_{in}, whereas in the higher frequency range, JL_{out} and JL_{in} are both pronounced. Figure 31(*c*) shows a wavepacket (denoted as SL_{KH}) distributed parallel to the SL. Because the shearing effect dominates in this region, we can infer that this structure is caused by the Kelvin–Helmholtz (KH) instability triggered by shearing across the air–water interface. Similar KH-induced wave structures near this region in ventilated cavities have been observed in previous experimental results (see e.g. Wu *et al.* 2019). Moreover, inside the cavity, we observe wavepackets (denoted as JL_r) that are distributed irregularly near the left branch of the JL, as shown in figure 31(*c*). These structures are associated with the re-entrant vortices, which are generated by the turbulent mixing in the closure region and are convected upstream due to the strong pressure gradient.

In summary, the results in figure 31 and the SPOD analysis lead to the following conclusions. First, coherent structures that are associated with different mechanisms are
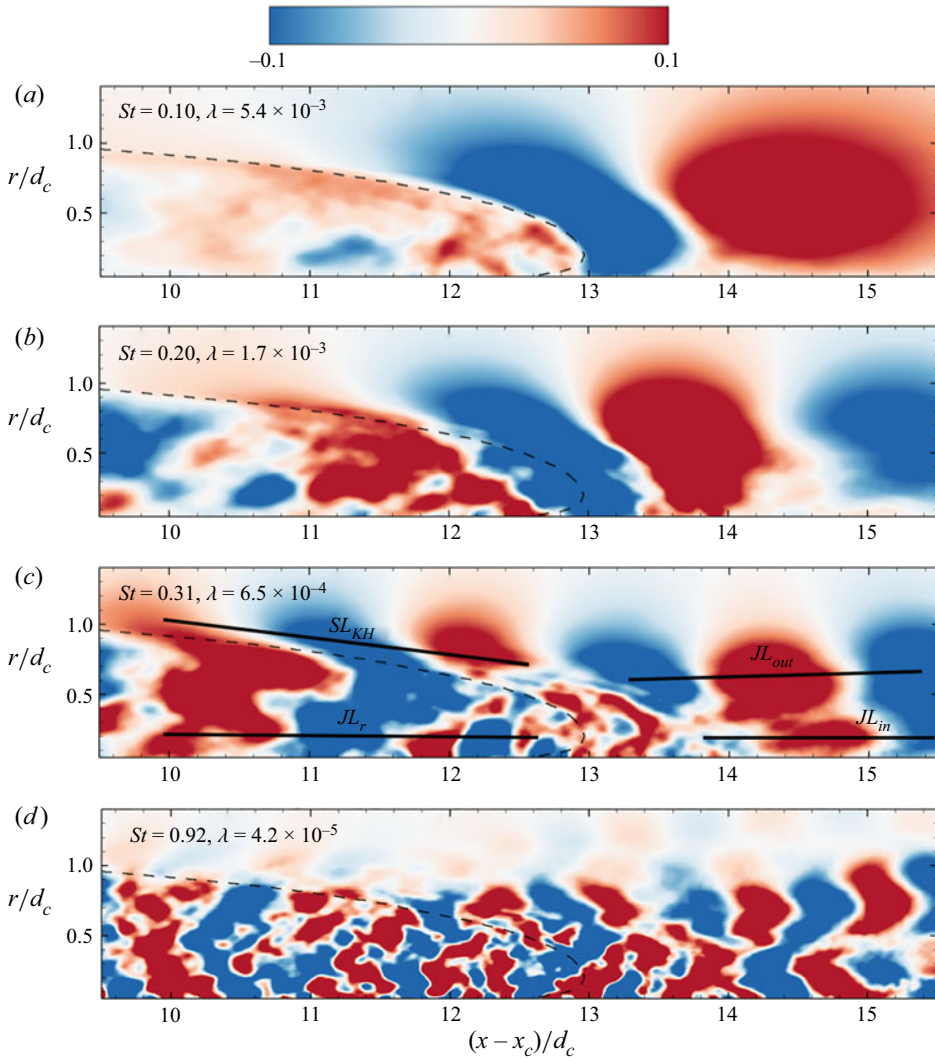
Figure 31. Contours of the real part of the normalized first SPOD mode for the radial velocity, $\Phi_r^{(1)}(x, r, St)/\|\Phi_r^{(1)}(x, r, St)\|_\infty$, in the domain D_t: (a) $St = 0.10$, (b) $St = 0.20$, (c) $St = 0.31$, and (d) $St = 0.92$. The black dashed lines are the isolines of $\bar{\phi} = 0.5$. The black solid lines in (c) indicate the observed wavepackets, including SL_{KH}, JL_r, JL_{out} and JL_{in}.

observed, including SL_{KH} induced by KH instability, SL_{out} associated with large-scale vortex shedding, SL_{in} associated with small-scale vortex shedding, and SL_r associated with the upstream convection of the more developed turbulence. Second, at the characteristic frequency $St = 0.1$, JL_{out} plays a dominant role in the flow dynamics. Finally, the SL_{KH} results agree with previous experimental findings.

7. Assessment of low-Reynolds-number DNS for insights into ventilated cavitating flows

In the present study, idealized DNS of ventilated cavitating flows with a Reynolds number of $O(10^3)$ are conducted, neglecting both gravity and interfacial tension effects. Previous

966 A20-34

experimental research, such as the study by Mäkiharju *et al.* (2013), has shown that the Reynolds number can impact the dynamics of ventilated cavity flows. In order to understand the implications of the low Reynolds number employed in the present DNS approach, a critical assessment of the fidelity of the model with respect to realistic flows is presented in this section.

Addressing the limitations of the present study is essential for understanding the extent to which the simulation results represent actual flow physics. In their comprehensive experimental work, Mäkiharju *et al.* (2013) investigated air entrainment at the closure of a wall bounded partial cavity ventilated with air injection, examining geometrically similar flows over a range of Reynolds numbers, from 10^6 to 10^7. They conducted Froude-scaled experiments with a Weber number variation of two orders of magnitude (10^3 to 10^5), observing significant variations in cavity interface patterns, closure topology, and gas entrainment rates. They found that lower *Re* cases exhibited glassy cavity interfaces, while higher *Re* cases showed stronger interactions with the turbulent flow of the liquid near the interface. The limitations of the current DNS study arise primarily from the lower Reynolds number, which may not capture the complex interactions between the liquid and gas phases at the realistic intensity. Moreover, neglecting the gravity and surface tension effects could affect the results' applicability to real-world scales and geometries. Consequently, further investigation at higher Reynolds numbers and incorporating other relevant effects, such as the Froude number and Weber number, is necessary for a more comprehensive understanding of ventilated cavitating flows.

Although the Reynolds number in the current study is lower than realistic values, the DNS can still provide valuable insights into the fundamental dynamics of ventilated cavitating flows and their interaction with turbulence. For example, several studies have examined the effects of the Reynolds number in breaking wave flows, focusing on key properties such as viscous dissipation, penetration depth, and transition from planar to three-dimensional flow. Deane, Stokes & Callaghan (2016) discussed turbulence saturation, where the increase in plume cross-sectional area is more relevant than the increase in fluid shear stress within the plume. Giorgio, Pirozzoli & Iafrati (2022) corroborated the findings that the dissipated energy fraction does not depend much on the Reynolds number or dimensionality. Mostert, Popinet & Deike (2022) observed that the Reynolds number does not affect the shape of the bubble size distribution after *Re* reaches a threshold, as the mean turbulent dissipation rate is not sensitive to *Re*. The ventilated cavity flows discussed in the present study and the wave breaking flows are both air–water turbulent mixed flow systems. Although their physics are different, findings from breaking wave studies can offer valuable insights for ventilated cavity studies. Based on the findings of Deane *et al.* (2016), Giorgio *et al.* (2022) and Mostert *et al.* (2022), the mean volume fraction of air, the mean velocity, and the pressure distributions inside the cavity obtained in the present study may help the understanding of the underlying dynamics of these flow processes. Moreover, the present DNS may provide valuable information on the flow dynamics and turbulence through detailed analyses, including vortex dynamics, Reynolds stresses, TKE generation and transport, air leakage and vortex shedding processes, and the relationships between gas exchange, vortical flow and Reynolds stress.

In summary, the low-Reynolds-number simulations in the present study hold the potential of shedding light on the fundamental dynamics of ventilated cavitating flows. Recognizing the limitations imposed by the chosen Reynolds number and the neglect of the effects of surface tension and gravity, it is important for future investigations into ventilated cavitating flows to consider these effects. By considering both the strengths and limitations of the current study, future studies can better understand the complex nature of this type of flow, and continue to advance the field.

8. Conclusions

In this work, we performed DNS studies with corresponding evaluations of discretization correlating to turbulent character to study ventilated cavitating flows. The interface between the air and water phases was captured by the CLSVOF method, which can describe accurately the interface geometry, shows good mass conservation performance, and captures robustly the dynamics of the two-phase flow. The essential non-oscillatory scheme was applied to the advection terms to improve the numerical accuracy. The cavitator body was represented using an immersed boundary method. The DNS results provide detailed descriptions of turbulent ventilated cavitating flows. Our analyses focus on the fundamental dynamics of the interaction between turbulence and ventilated cavitation.

Based on the DNS data, temporal and azimuthal averaging were employed to calculate the mean volume fraction of the fluid phases and the mean velocity. The mean volume fraction of air was approximately 0.5 in most of the closure region of the cavity due to the violent mixing of air and water.

At the front part of the cavity, the streamwise flow dominates over the radial flow. The mean streamwise velocity indicates several characteristic flow structures, including the shear layer (SL) structure, where the air is sheared by the outside water flow and moves forwards, and the recirculation area (RA), where the air travels backwards into the cavitator and decelerates. Moreover, in the closure region of the cavity, the water jet flow behind the SL, i.e. the jet layer (JL), is another characteristic structure, where one branch of the jet moves backwards and re-enters the bubble, while the other branch moves forwards into the wake. The pressure distributions inside the cavity and near the closure region were studied by examining the mean cavitation number along the central axis, which maintains a constant value of approximately $\sigma = 0.15$ and then decreases sharply near the closure region due to the stagnation zone inside the JL structure. The variations in the cavitation number and the cavity profile are consistent with existing semi-empirical theories.

The mean enstrophy and its components were analysed to elucidate the vortex dynamics in the cavitating flow. The results show that the enstrophy is contributed mainly by the transverse vorticity component due to the shear effect between the air and water, which is concentrated in the SL at the front part of the cavity and throughout the whole closure region. The streamwise component of the enstrophy is negligible at the front part but increases in the closure region. The vortex dynamics in the cavity was also investigated by studying the enstrophy budget equation. We emphasized evaluating the terms that govern the vorticity generation, i.e. the stretching effect term, baroclinic effect term and viscous effect term. At the front part of the cavity, the vortex dynamics are governed by all three effects, while in the closure region, the vortex dynamics is dominated by baroclinic and viscous effects.

Moreover, a study of the Reynolds stresses suggested that the streamwise component, whose peak value occurs near the air–water interface, dominates the other components in most of the cavity. Overall, the Reynolds stresses become stronger near the closure region, where the diagonal components are comparable, indicating that the flow becomes isotropic in this region.

Furthermore, we found that the TKE is large near the closure region of the cavity, especially within the JL structure. Moreover, in both the SL and JL structures, streamwise turbulent fluctuations dominate transverse fluctuations. In addition, the SL and JL structures play different roles in the generation and transport of TKE. In the SL structure, the TKE is increased by the production transport term due to shear effects, while in the JL structure, the TKE decreases due to streamwise stretching effects. In both the SL and JL,

the pressure transport term tends to enhance the TKE. Moreover, the mean flow advective transport and pressure transport terms are conducive to transporting TKE from the SL to the JL.

The air leakage and vortex shedding processes in the closure region were also investigated. The generation of vortex structures is associated with the leakage of air bubbles. In addition, these processes occur in a stagnant high-pressure region where the air and water phases mix violently and turbulently. Moreover, the frequency spectra of the velocity and VOF function of water near the closure region were calculated. The vortex shedding in the closure region shows a semi-periodic pattern, and the energy spectra show an intrinsic characteristic frequency. The autocorrelation function of the volume fraction of air in a control volume in the closure region demonstrates that the air leakage and vortex shedding processes have the same characteristic frequency.

To study further the structures near the closure region, and connect these structures to the vortex shedding and air leakage processes, we performed SPOD analyses to identify coherent structures oscillating at different frequencies. The cumulative fraction of energy results indicate that the first SPOD mode contributes more to the energy than the remaining modes, especially in the low-frequency range, indicating a low-rank behaviour. The relative contribution by the leading mode increases with increasing downstream distance. Moreover, the contours of the first SPOD mode for the radial velocity at different frequencies show that various coherent structures are associated with different mechanisms near the closure region, including SL_{KH} induced by KH instability, SL_{out} associated with large-scale vortex shedding, SL_{in} associated with small-scale vortex shedding, and SL_r associated with the upstream turbulent convection. Near the characteristic frequency $St = 0.1$, the JL_{out} structure plays a dominant role in the dynamics.

We note that the present study uses an incompressible flow model and does not consider compressibility effects. A study by Ganesh, Mäkiharju & Ceccio (2016) showed that the formation and propagation of bubbly shocks can play an important role in the dynamics of the cavity. Their study indicates that cavitating flows with volume fractions of the order of 0.1 have low sound speeds and relatively high Mach numbers. The resulting formation and propagation of bubbly shocks has a considerable influence on the dynamics of the cavity. Additionally, bubbly shocks can change the pattern of the closure. Their study noted two different mechanisms associated with shedding cavities in unsteady cavitating flows: RJ-induced shedding, and bubbly shock propagation, which shows strong, periodic cloud shedding behaviours. Their results indicate that models for the dynamics of cavities and closures need to be improved by incorporating the bubbly shock effect. In addition, Ganesh *et al.* (2016) found that analytical models and basic jump relations associated with one-dimensional bubbly shock propagation can capture essential cavity dynamics.

In cavitating flows, there exist turbulent motions over a wide range of scales, violent mixing between the air and water, and interactions between different characteristic structures. High-fidelity numerical simulations complement experimental research by providing non-intrusive methods for describing flow fields in detail. This work is DNS with reasonable practice. In future work, to perform more realistic numerical simulations and improve the role of these simulations in studying ventilated cavitation problems, the following topics should be considered. First, Reynolds numbers higher than those employed in the present study need to be considered in future applications. Second, we emphasize that the problem studied is artificial cavitation, not natural cavitation. Future simulations should consider the effects of natural cavitation to investigate its influence on the dynamics in ventilated cavitating flows. Moreover, an appropriate two-phase subgrid-scale turbulence model should be developed for large-eddy simulations

of cavitating flows. Additionally, reduced-order models need to be established based on the characteristics of the SL and JL structures for applications such as the optimization of supercavities. Moreover, the relationship among the gas exchange, vortical flow in the closure, and Reynolds stress needs to be studied further by performing more simulations with a wider range of parameters. Furthermore, future simulations should consider compressibility to study the effects of bubbly shocks on cavities (Ganesh *et al.* 2016).

Supplementary movies. A supplementary movie is available at https://doi.org/10.1017/jfm.2023.431.

Declaration of interests. The authors report no conflict of interest.

Author ORCIDs.

Ⓑ Han Liu https://orcid.org/0000-0002-7533-3454;

Ⓑ Zuoli Xiao https://orcid.org/0000-0001-6123-3404;

Ⓑ Lian Shen https://orcid.org/0000-0003-3762-3829.

Appendix A. Validation and resolution test

The computational methods employed in the present study have been validated extensively by our group in previous research on other multifluid problems (e.g. Hu *et al.* 2012; Yang *et al.* 2017, 2018; Gao *et al.* 2021*a,b*). To validate further the applicability of the numerical schemes in addressing the present ventilated cavitation problem, we have performed more tests by making comparisons of our results with the results in the literature, and conducted grid convergence tests. Note that although our simulation considers viscous effects by solving the Navier–Stokes equations, the front geometry of the cavity is dominated mainly by the inviscid flow dynamics, which validates the following comparison between our CFD results and the potential flow theory.

Brennen (1969) studied the blockage effect on the minimal cavitation number σ_{min} based on potential flow theory, where σ_{min} is approached at large C_q values. In our numerical tests, we used three sets of grids with different resolutions, namely $\Delta x_{min}/d_c = 0.08$, $\Delta x_{min}/d_c = 0.04$ and $\Delta x_{min}/d_c = 0.02$. Figure 32 shows that when the mesh is refined, the σ_{min} value calculated according to our simulations approaches the prediction of Brennen (1969). The result indicates that the grid resolution of $\Delta x_{min}/d_c = 0.02$ is sufficient to capture accurately the cavity for $B < 18\%$. We also conducted simulations using the same parameter values as those in the Cao *et al.* (2017) experiment, namely $B = 9\%$, $C_q = 0.14$ and $Fr = 18$. Figure 33 compares the cavity profiles. Our result is consistent with the experimental profiles in the front part of the cavity.

To verify the convergence for the three grids used in the present study, the mean flow and the turbulence statistics of the simulations on a coarse grid M_1, intermediate grid M_2, and fine grid M_3 are compared. The details of the grids M_1, M_2 and M_3 are provided in § 2.3. Figure 34 shows that the discrepancy in the isolines $\bar{\phi} = 0.5$ between the M_2 and M_3 simulations is considerably smaller than that between the M_1 and M_2 simulations, which indicates a trend to converge when the mesh grid is refined.

Figure 35 plots the mean flow and turbulence statistics along the streamwise axis, including the averaged VOF function $\bar{\phi}$, mean streamwise velocity $\bar{u}$, streamwise turbulent fluctuation $\overline{u'u'}$, and turbulent energy dissipation rate ϵ. The first-order statistics ($\bar{\phi}$ and $\bar{u}$) and second-order statistics ($u'u'$ and ϵ) are both captured qualitatively by the simulations using the mesh grids M_1, M_2 and M_3. The discrepancies between the results using grids M_2 and M_3 are substantially smaller than the discrepancies between the results using grids M_1 and M_2, which again shows a trend to converge when the mesh grid is refined.
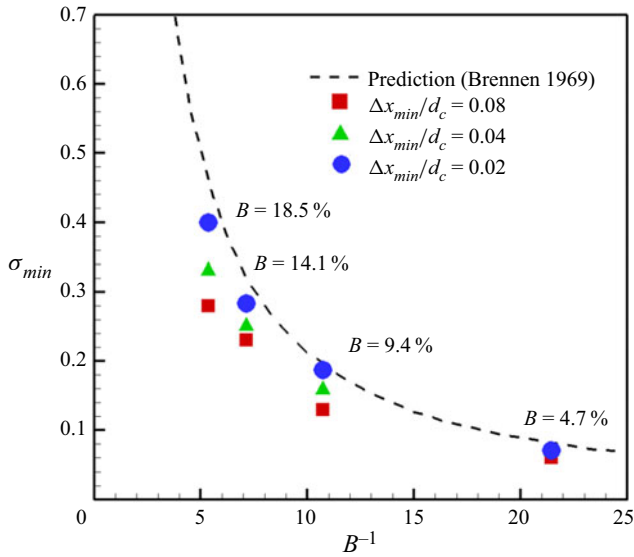
Figure 32. Predicted minimal cavitation number σ_{min} for a given blockage ratio B. The red squares, green triangles and blue circles correspond to the simulation results using coarse, medium and refined grids, respectively. The black dashed line corresponds to the formula from the theory of Brennen (1969).
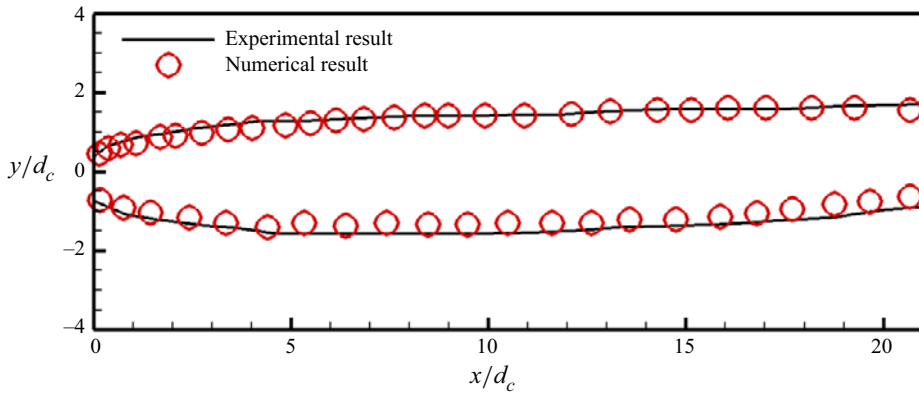

Figure 33. Comparison of the cavity profiles in the Cao *et al.* (2017) experiment (red circles) and the present simulation (black solid lines). The parameters are set to $B = 9\%$, $C_q = 0.14$ and $Fr = 18$.
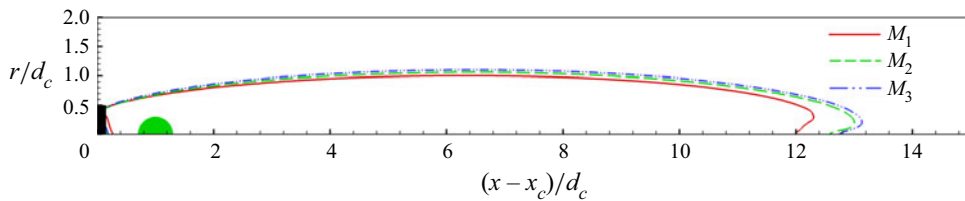

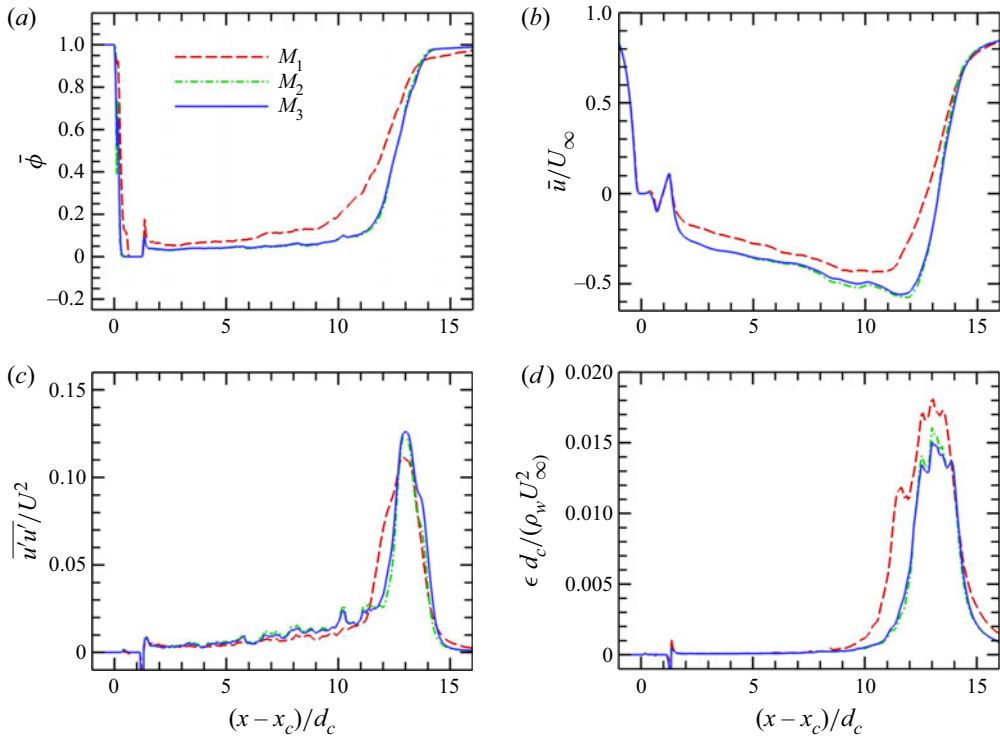Figure 34. Comparison of the isolines of $\bar{\phi} = 0.5$ in the simulations with grids M_1, M_2 and M_3.

966 A20-39

Figure 35. Grid convergence results for multiphase turbulent flow statistics: (*a*) $\bar{\phi}$, (*b*) $\bar{u}$, (*c*) $u'u'$, and (*d*) ϵ.

The differences in the results between grids M_2 and M_3 are negligibly small, indicating numerical convergence.

To confirm that the mesh resolution employed in the present study is sufficient to capture the turbulence dynamics in the closure region of the ventilated cavity, we calculate the smallest scale of the turbulent eddies, i.e. the Kolmogorov length scale, which is defined as (Kolmogorov 1941)

$$\eta = \left(\frac{\nu}{\epsilon/\rho} \right)^{1/4}. \tag{A1}$$

Based on the criterion given by Pope (2000), simulations can be considered DNS with the Kolmogorov scale η resolved if the ratio of the local cell size Δ to η satisfies $\Delta/\eta < 2.1$. Figure 36 plots Δ/η in the closure region of the cavity according to simulations using mesh grids M_1, M_2 and M_3. The results show that the Δ/η ratio in the M_3 simulation satisfies $\Delta/\eta < 2.1$, while the Δ/η ratios in the M_1 and M_2 simulations show some areas with $\Delta/\eta \geq 2.1$ in the closure region. In this paper, the data obtained on the fine grid M_3 are used in the analyses and discussions.

Appendix B. Quadrant analysis of the Reynolds shear stress

To examine further the Reynolds shear stress τ_{xr}^R shown in figure 14(*d*), we perform a quadrant analysis to illustrate the contributions by four different quadrants of τ_{xr}^R, which are classified according to the signs of the velocity fluctuations: $Q_1(+\sqrt{\rho}\,u_x'', +\sqrt{\rho}\,u_r'')$, $Q_2(-\sqrt{\rho}\,u_x'', +\sqrt{\rho}\,u_r'')$, $Q_3(-\sqrt{\rho}\,u_x'', -\sqrt{\rho}\,u_r'')$, and
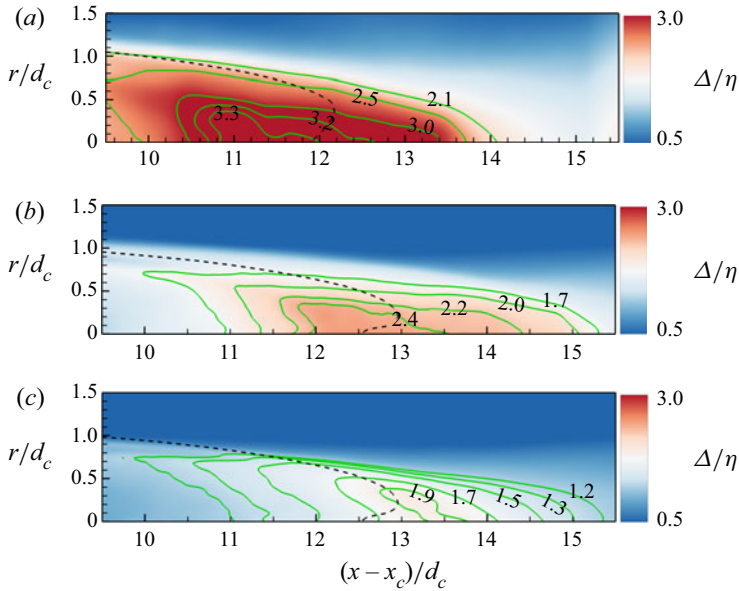
966 A20-40

Figure 36. Contours of the ratio of the local cell size to the Kolmogorov scale, Δ/η, on (*a*) grid M_1, (*b*) grid M_2, and (*c*) grid M_3. The black dashed line corresponds to the isoline of $\bar{\phi} = 0.5$.
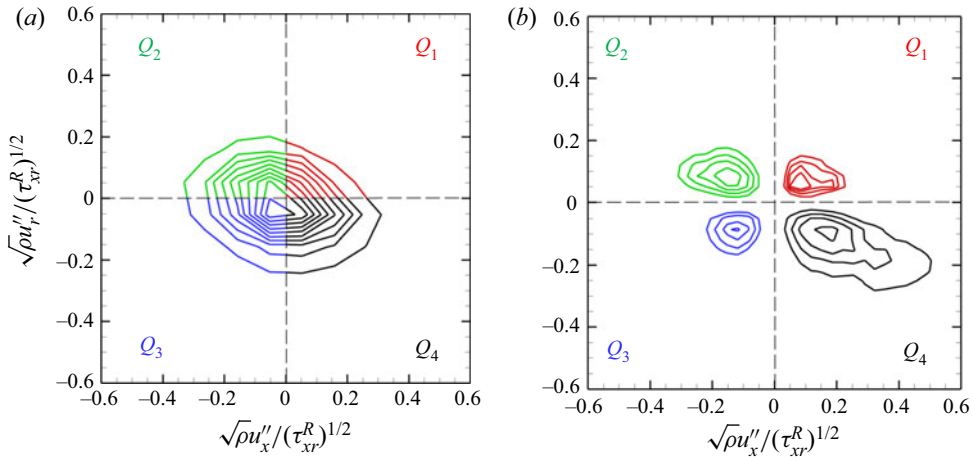

Figure 37. Isocontours of (*a*) the joint probability distribution function $P(\sqrt{\rho}\,u_x'', \sqrt{\rho}\,u_r'')$, and (*b*) the covariance integrand $\rho u_x'' u_r'' P(\sqrt{\rho}\,u_x'', \sqrt{\rho}\,u_r'')$, at the location where τ_{xr}^R reaches its peak value. The contour intervals in (*a*) and (*b*) are $[0.01, 0.1]$ and $[0.02, 0.1]$, respectively.

$Q_4(+\sqrt{\rho}\,u_x'', -\sqrt{\rho}\,u_r'')$ (Wallace 2016). Figures 37(*a*) and 37(*b*) present the joint probability distribution function $P(\sqrt{\rho}\,u_x'', \sqrt{\rho}\,u_r'')$ and the covariance integrand $\rho u_x'' u_r'' P(\sqrt{\rho}\,u_x'', \sqrt{\rho}\,u_r'')$, respectively, which are obtained at the location where τ_{xr}^R obtains its peak value. Figure 37(*a*) shows that the major axis of the elliptically shaped $P(\sqrt{\rho}u_x'', \sqrt{\rho}u_r'')$ is inclined towards Q_4 and Q_2. Additionally, the covariance integrand shown in figure 37(*b*) indicates that the Q_2 and Q_4 quadrants contribute more to the Reynolds shear stress τ_{xr}^R than the Q_1 and Q_3 quadrants.

REFERENCES

ABRAHAM, N.V., JAMES, S.U. & IVAN, N.K. 2003 High-speed bodies in partially cavitating axisymmetric flow. In *Proceedings of the Fifth International Symposium on Cavitation, Osaka, Japan*.

ABREU, L.I., CAVALIERI, A.V., SCHLATTER, P., VINUESA, R. & HENNINGSON, D.S. 2020 Spectral proper orthogonal decomposition and resolvent analysis of near-wall coherent structures in turbulent pipe flows. *J. Fluid Mech.* **900**, A11.

AHN, B.K., JEONG, S.W., KIM, J.H., SHAO, S., HONG, J. & ARNDT, R.E.A. 2017 An experimental investigation of artificial supercavitation generated by air injection behind disk-shaped cavitators. *Intl J. Nav. Archit.* **9** (2), 227–237.

ARNDT, R.E. 2002 Cavitation in vortical flows. *Annu. Rev. Fluid Mech.* **34** (1), 143–175.

AUBRY, N. 1991 On the hidden beauty of the proper orthogonal decomposition. *Theor. Comput. Fluid Dyn.* **2** (5), 339–352.

BALAY, S., ABHYANKAR, S., ADAMS, M., BROWN, J., BRUNE, P., BUSCHELMAN, K., DALCIN, L.D., EIJKHOUT, V., GROPP, W. & KAUSHIK, D. 2017 PETSc users' manual revision 3.8. *Tech. Rep.* Argonne National Laboratory (ANL).

BARBACA, L., PEARCE, B.W., GANESH, H., CECCIO, S.L. & BRANDNER, P.A. 2019 On the unsteady behaviour of cavity flow over a two-dimensional wall-mounted fence. *J. Fluid Mech.* **874**, 483–525.

BERKOOZ, G., HOLMES, P. & LUMLEY, J.L. 1993 The proper orthogonal decomposition in the analysis of turbulent flows. *Annu. Rev. Fluid Mech.* **25** (1), 539–575.

BRENNEN, C. 1969 A numerical solution of axisymmetric cavity flows. *J. Fluid Mech.* **37**, 671–688.

BROUZET, D., HAGHIRI, A., TALEI, M., BREAR, M.J., SCHMIDT, O.T., RIGAS, G. & COLONIUS, T. 2020 Role of coherent structures in turbulent premixed flame acoustics. *AIAA J.* **58** (6), 2635–2642.

CALLENAERE, M., FRANC, J.P., MICHEL, J.M. & RIONDET, M. 2001 The cavitation instability induced by the development of a re-entrant jet. *J. Fluid Mech.* **444**, 223–256.

CAMPBELL, I.J. & HILBORNE, D.V. 1958 Air entrainment behind artificially inflated cavities. In *Proceedings of the Second Symposium on Naval Hydrodynamics, Washington, DC, USA*. Office of Naval Research.

CAO, L., KARN, A., ARNDT, R.E.A., WANG, Z. & HONG, J. 2017 Numerical investigations of pressure distribution inside a ventilated supercavity. *J. Fluid Engng* **139** (2), 021301.

COX, R.N. & CLAYDEN, W.A. 1956 Air entrainment at the rear of a steady cavity. In *Proceedings of the Symposium on Cavitation in Hydrodynamics, London, UK*. National Physical Laboratory.

CUI, Z., YANG, Z., JIANG, H., HUANG, W. & SHEN, L. 2018 A sharp-interface immersed boundary method for simulating incompressible flows with arbitrarily deforming smooth boundaries. *Intl J. Comput. Meth.* **15**, 1750080.

DEANE, G.B., STOKES, M.D. & CALLAGHAN, A.H. 2016 The saturation of fluid turbulence in breaking laboratory waves and implications for whitecaps. *J. Phys. Oceanogr.* **46** (3), 975–992.

DITTAKAVI, N., CHUNEKAR, A. & FRANKEL, S. 2010 Large eddy simulation of turbulent–cavitation interactions in a Venturi nozzle. *Trans. ASME J. Fluids Engng* **132**, 121301.

EPSHTEIN, L.A. 1973 Characteristics of ventilated cavities and some scale effects. In *Proceedings of the International Symposium IUTAM, Unsteady Water Flow with High Velocities, Nauka, Japan*.

GANESH, H., MÄKIHARJU, S.A. & CECCIO, S.L. 2016 Bubbly shock propagation as a mechanism for sheet-to-cloud transition of partial cavities. *J. Fluid Mech.* **802**, 37–78.

GAO, Q., DEANE, G., LIU, H. & SHEN, L. 2021*a* A robust and accurate technique for Lagrangian tracking of bubbles and drops and detecting fragmentation and coalescence. *Intl J. Multiphase Flow* **135**, 103523.

GAO, Q., DEANE, G.B. & SHEN, L. 2021*b* Bubble production by air filament and cavity breakup in plunging breaking wave crests. *J. Fluid Mech.* **929**, A44.

GHATE, A.S., TOWNE, A. & LELE, S.K. 2020 Broadband reconstruction of inhomogeneous turbulence using spectral proper orthogonal decomposition and Gabor modes. *J. Fluid Mech.* **888**, R1.

GIORGIO, S.D., PIROZZOLI, S. & IAFRATI, A. 2022 On coherent vortical structures in wave breaking. *J. Fluid Mech.* **947**, A44.

GNANASKANDAN, A. & MAHESH, K. 2016 Numerical investigation of near-wake characteristics of cavitating flow over a circular cylinder. *J. Fluid Mech.* **790**, 453–491.

GOPALAN, S. & KATZ, J. 2000 Flow structure and modeling issues in the closure region of attached cavitation. *Phys. Fluids* **12** (4), 895–911.

HALLER, G. 2005 An objective definition of a vortex. *J. Fluid Mech.* **525**, 1–26.

HELLSTRÖM, L.H., GANAPATHISUBRAMANI, B. & SMITS, A.J. 2015 The evolution of large-scale motions in turbulent pipe flow. *J. Fluid Mech.* **779**, 701–715.

HU, Y., GUO, X., LU, X., LIU, Y., DALRYMPLE, R.A. & SHEN, L. 2012 Idealized numerical simulation of breaking water wave propagating over a viscous mud layer. *Phys. Fluids* **24** (11), 112104.

IYER, C.O. & CECCIO, S.L. 2002 The influence of developed cavitation on the flow of a turbulent shear layer. *Phys. Fluids* **14** (10), 3414–3431.

JIANG, Y., SHAO, S. & HONG, J. 2018 Experimental investigation of ventilated supercavitation with gas jet cavitator. *Phys. Fluids* **30** (1), 012103.

KADU, P.A., SAKAI, Y., ITO, Y., IWANO, K., SUGINO, M., KATAGIRI, T., HAYASE, T. & NAGATA, K. 2020 Application of spectral proper orthogonal decomposition to velocity and passive scalar fields in a swirling coaxial jet. *Phys. Fluids* **32** (1), 015106.

KARATHANASSIS, I.K., KOUKOUVINIS, P., KONTOLATIS, E., LEE, Z., WANG, J., MITROGLOU, N. & GAVAISES, M. 2018 High-speed visualization of vortical cavitation using synchrotron radiation. *J. Fluid Mech.* **838**, 148–164.

KARN, A., ARNDT, R.E.A. & HONG, J. 2016 An experimental investigation into supercavity closure mechanisms. *J. Fluid Mech.* **789**, 259–284.

KAWAKAMI, E. & ARNDT, R.E.A. 2011 Investigation of the behavior of ventilated supercavities. *J. Fluid Engng* **133** (9), 091305.

KIM, W. & CHOI, H. 2019 Immersed boundary methods for fluid–structure interaction: a review. *Intl J. Heat Fluid Flow* **75**, 301–309.

KIM, J. & MOIN, P. 1985 Application of a fractional-step method to incompressible Navier–Stokes equations. *J. Comput. Phys.* **59**, 308–323.

KINZEL, M.P. 2008 Computational techniques and analysis of cavitating-fluid flows. PhD thesis, Pennsylvania State University, PA.

KINZEL, M.P., LINDAU, J. & KUNZ, R. 2009 Air entrainment mechanisms from artificial supercavities: insight based on numerical simulations. In *Proceedings of the Seventh International Symposium on Cavitation, (CAV2009), Ann Arbor, MI, USA*, vol. 136.

KOLMOGOROV, A.N. 1941 Local structure of turbulence in an incompressible fluid for very large Reynolds numbers. *Dokl. Akad. Nauk SSSR* **30**, 299–303.

KOUKOUVINIS, P., MITROGLOU, N., GAVAISES, M., LORENZI, M. & SANTINI, M. 2017 Quantitative predictions of cavitation presence and erosion-prone locations in a high-pressure cavitation test rig. *J. Fluid Mech.* **819**, 21–57.

KUNZ, R.F., BOGER, D.A., STINEBRING, D.R., CHYCZEWSKI, T.S., LINDAU, J.W., GIBELING, H.J., VENKATESWARAN, S. & GOVINDAN, T.R. 2000 A preconditioned Navier–Stokes method for two-phase flows with application to cavitation prediction. *Comput. Fluids* **29** (8), 849–875.

LI, X.B., CHEN, G., LIANG, X.F., LIU, D.R. & XIONG, X.H. 2021 Research on spectral estimation parameters for application of spectral proper orthogonal decomposition in train wake flows. *Phys. Fluids* **33** (12), 125103.

LINDAU, J., SKIDMORE, G., BRUNGART, T., MOENY, M. & KINZEL, M.P. 2015 Finite volume computation of the mitigation of cavity pulsation. In *Proceedings of the Ninth International Symposium on Cavitation, (CAV2015), Lausanne, Switzerland*, vol. 656.

LING, Y., FUSTER, D., TRYGGVASON, G. & ZALESKI, S. 2019 A two-phase mixing layer between parallel gas and liquid streams: multiphase turbulence statistics and influence of interfacial instability. *J. Fluid Mech.* **859**, 268–307.

LIU, H. & XIAO, Z. 2016 Scale-to-scale energy transfer in mixing flow induced by the Richtmyer–Meshkov instability. *Phys. Rev.* E **93** (5), 053112.

LODATO, G., DOMINGO, P. & VERVISCH, L. 2008 Three-dimensional boundary conditions for direct and large-eddy simulation of compressible viscous flows. *J. Comput. Phys.* **227** (10), 5105–5143.

LOGVINOVICH, G. 1973 Hydrodynamics of free-boundary flows. *Tech. Rep.* National Advisory Committee for Aeronautics.

LUMLEY, J.L. 1967 The structure of inhomogeneous turbulent flows. In *Atmospheric Turbulence and Radio Wave Propagation* (ed. A.M. Yaglom & V.I. Tatarski), pp. 166–178. Nauka.

LUMLEY, J.L. 1970 *Stochastic Tools in Turbulence*. Academic.

MÄKIHARJU, S.A., ELBING, B.R., WIGGINS, A., SCHINASI, S., BROECK, J.M.V., PERLIN, M., DOWLING, D.R. & CECCIO, S.L. 2013 On the scaling of air entrainment from a ventilated partial cavity. *J. Fluid Mech.* **732**, 47–76.

MEYER, K.E., PEDERSEN, J.M. & ÖZCAN, O. 2007 A turbulent jet in crossflow analysed with proper orthogonal decomposition. *J. Fluid Mech.* **583**, 199–227.

MIN, C. 2010 On reinitializing level set functions. *J. Comput. Phys.* **229** (8), 2764–2772.

MITTAL, R. & IACCARINO, G. 2005 Immersed boundary methods. *Annu. Rev. Fluid Mech.* **37** (1), 239–261.

MOIN, P. & MAHESH, K. 1998 Direct numerical simulation: a tool in turbulence research. *Annu. Rev. Fluid Mech.* **30** (1), 539–578.

MOSTERT, W., POPINET, S. & DEIKE, L. 2022 High-resolution direct simulation of deep water breaking waves: transition to turbulence, bubbles and droplets production. *J. Fluid Mech.* **942**, A27.

NEKKANTI, A. & SCHMIDT, O.T. 2021 Frequency–time analysis, low-rank reconstruction and denoising of turbulent flows using SPOD. *J. Fluid Mech.* **926**, A26.

NIDHAN, S., SCHMIDT, O.T. & SARKAR, S. 2022 Analysis of coherence in turbulent stratified wakes using spectral proper orthogonal decomposition. *J. Fluid Mech.* **934**, A12.

PLESSET, M.S. & PROSPERETTI, A. 1977 Bubble dynamics and cavitation. *Annu. Rev. Fluid Mech.* **9** (1), 145–185.

POPE, S.B. 2000 *Turbulent Flows*, 1st edn. Cambridge University Press.

ROOD, E.P. 1991 Mechanisms of cavitation inception. *Trans. ASME J. Fluids Engng* **113**, 163–175.

SCHMIDT, O.T. & COLONIUS, T. 2020 Guide to spectral proper orthogonal decomposition. *AIAA J.* **58** (3), 1023–1033.

SCHMIDT, O.T., TOWNE, A., RIGAS, G., COLONIUS, T. & BRÈS, G.A. 2018 Spectral analysis of jet turbulence. *J. Fluid Mech.* **855**, 953–982.

SEMENENKO, V.N. 2001 *Artificial Supercavitation: Physics and Calculation*. Ukrainian Academy of Sciences, Kiev Institute of Hydromechanics.

SENOCAK, I. & SHYY, W. 2002 A pressure-based method for turbulent cavitating flow computations. *J. Comput. Phys.* **176** (2), 363–383.

SHAO, S., KARN, A., AHN, B.K., ARNDT, R.E.A. & HONG, J. 2017 A comparative study of natural and ventilated supercavitation across two closed-wall water tunnel facilities. *Exp. Therm. Fluid Sci.* **88**, 519–529.

SHU, C.W. & OSHER, S. 1989 Efficient implementation of essentially non-oscillatory shock-capturing schemes, I. *J. Comput. Phys.* **83** (1), 32–78.

SIROVICH, L. 1987 Turbulence and the dynamics of coherent structures. I. Coherent structures. *Q. Appl. Maths* **45** (3), 561–571.

SPURK, J.H. 2002 On the gas loss from ventilated supercavities. *Acta Mechanica* **155** (3), 125–135.

SUSSMAN, M. & PUCKETT, E.G. 2000 A coupled level set and volume of fluid method for computing 3D and axisymmetric incompressible two-phase flows. *J. Comput. Phys.* **162** (2), 301–337.

SUSSMAN, M., SMEREKA, P. & OSHER, S. 1994 A level set approach for computing solutions to incompressible two-phase flow. *J. Comput. Phys.* **114** (1), 146–159.

TOWNE, A., SCHMIDT, O.T. & COLONIUS, T. 2018 Spectral proper orthogonal decomposition and its relationship to dynamic mode decomposition and resolvent analysis. *J. Fluid Mech.* **847**, 821–867.

UHLMAN, J.S. & JAMES, S. 1989 Supercavitating hydrofoils. *J. Ship Res.* **33** (1), 16–20.

WALLACE, J.M. 2016 Quadrant analysis in turbulence research: history and evolution. *Annu. Rev. Fluid Mech.* **48**, 131–158.

WANG, Z., LIU, H., GAO, Q., WANG, Z., WANG, Y., WANG, G. & SHEN, L. 2021*a* Numerical investigation of ventilated cavitating flow in the wake of a circular cylinder. *Phys. Rev. Fluids* **6** (6), 064303.

WANG, G. & OSTOJA-STARZEWSKI, M. 2007 Large eddy simulation of a sheet/cloud cavitation on a NACA0015 hydrofoil. *Appl. Math. Model.* **31** (3), 417–447.

WANG, Z., YANG, J., ANDERSSON, H.I., ZHU, X., LIU, M., WANG, L. & LU, X. 2021*b* Numerical investigation on the flow around an inclined prolate spheroid. *Phys. Fluids* **33** (7), 074106.

WANG, Z., ZHANG, M., KONG, D., HUANG, B., WANG, G. & WANG, C. 2018 The influence of ventilated cavitation on vortex shedding behind a bluff body. *Exp. Therm. Fluid Sci.* **98**, 181–194.

WEYMOUTH, G.D. & YUE, D.K.-P. 2010 Conservative volume of fluid method for free-surface simulations on Cartesian-grids. *J. Comput. Phys.* **229** (8), 2853–2865.

WU, J., DEIJLEN, L., BHATT, A., GANESH, H. & CECCIO, S.L. 2021 Cavitation dynamics and vortex shedding in the wake of a bluff body. *J. Fluid Mech.* **917**, A26.

WU, Y., LIU, Y., SHAO, S. & HONG, J. 2019 On the internal flow of a ventilated supercavity. *J. Fluid Mech.* **862**, 1135–1165.

YANG, Z., DENG, B. & SHEN, L. 2018 Direct numerical simulation of wind turbulence over breaking waves. *J. Fluid Mech.* **850**, 120–155.

YANG, Z., LU, X.H., GUO, X., LIU, Y. & SHEN, L. 2017 Numerical simulation of sediment suspension and transport under plunging breaking waves. *Comput. Fluids* **158**, 57–71.

YOON, K., QIN, S., SHAO, S. & HONG, J. 2020 Internal flows of ventilated partial cavitation. *Exp. Fluids* **61**, 100.

ZHOU, J., YU, K., MIN, J. & YANG, M. 2010 The comparative study of ventilated super cavity shape in water tunnel and infinite flow field. *J. Hydrodyn.* B **22** (5), 689–696.